A novel micromechanical method for nonlinear analysis of magnetostrictive composites

Ziwei Li[a], Junjie Ye[a,c*], Yiwei Wang[a], Lu Liu[a], Yang Shi[a],

Yang Li[b], Jianqiao Ye[c*]

[a] Shaanxi Key Laboratory of Space Extreme Detection, Key Laboratory of Ministry of Education for Electronic Equipment Structure Design, Xidian University, Xi'an 710071, China

[b] China Academy of Space Technology (Xi'an), Xi'an, 710100,China

[c] School of Engineering, Lancaster University, Lancaster LA1 4YW, UK

Abstract:

In this paper, a novel micromechanical modeling framework is presented to investigate mechanical properties of a multiphase magnetostrictive composite subjected to a multi-field coupling environment. To this end, a nonlinear constitutive equation with consideration of mechanical-magneto-thermal condition is proposed. Parametric elements are used to discretize a representative volume element (RVE) of the material to obtain local stress distribution. The macroscopic strain responses of the magnetostrictive material under magnetic field loading are predicated considering local equilibrium and using the homogenization technique. Numerical results are compared with the available experimental data. In general, the proposed method offers a useful tool to study the effects of external pre-stress, ambient temperature and fiber volume fraction on the overall characteristics of fiber reinforced magnetostrictive composites. The numerical results show that the nonlinear variations of strain and flux density are closely related to the magnetization intensity.

Keywords: Magnetostrictive composites, Micromechanics, Nonlinear constitutive relation, Parametric finite-volume model

1. Introduction

Magnetostriction effect refers to a phenomenon that magnetostrictive materials produce elastic strain along the external magnetization direction when they are subjected to external magnetic field. Therefore, magnetostrictive materials show obvious magneto-elastic coupling effect, which can be used to covert magnetic energy to mechanical energy or verse vie. Owing to the magnetostrictive property, magnetostrictive materials have been widely used in the manufacturing process of actuators and sensors[1].

In general, magnetostrictive materials generate linear strain response under magnetic field. However, some magnetostrictive materials, such as Terfenol-D, exhibit strong nonlinear magneto-mechanical effect[2–4] due to complex environmental factors. Thus, an accurate nonlinear constitutive equation is required to predict their nonlinear magneto-mechanical property. Carman and Mitrovic[5] proposed a standard square model, and the numerical results were compared with experiment data. Wan et al.[6,7] proposed a hyperbolic tangent model that was used to simulate experimental results. Duenas et al.[8] used magnetization intensity instead of magnetic field intensity as the independent variable of magnetostrictive constitutive model to calculate the effective magnetostrictive properties. Zheng and Liu[9,10] established a new constitutive model based on the Gibbs free energy theory to investigate magnetostrictive strain under different magnetic field and pre-stress environments. Zheng and Jin[11]established a coupled mechanical-magnetic-thermal

constitutive model with consideration of temperature and hysteresis effects.

The nonlinear constitutive model mentioned above mainly focused on one-dimensional magnetostrictive rods or two-dimensional thin films. As a brittle material with a low modulus of elasticity, it is difficult to machine Terfenol-D and form monolithic magnetostrictive materials. To increase the potential of widening the use of the materials, some non-magnetic phase materials are added into the magnetostrictive phase to form a magnetostrictive composite. For instance, Terfenol-D particles or flakes are embedded into polymers (e.g., epoxy) or ceramic substrates (e.g., $BaTiO_3$) to improve their strength and toughness[12]. The effective properties of a magnetostrictive heterogeneous material depend on multiplefactors, such as volume fraction of individual components and microstructures[13]. Herbst et al.[14] established an approximate spherical model to predict effective magnetostriction of particle-reinforced composites. Nan and Weng[15,16] constructed a homogenization model by introducing two independent Green's functions to decouple the interactions between the magnetic and stress field. Liu et al.[17] studied the influences of inclusion shape, applied stress and matrix properties on the magnetostrictive properties of heterogeneous materials. However, all the above models were developed by assuming uniform stress distribution. Tang et al.[18] analyzed the influences of interfacial phase and constituent properties on magnetostriction using an asymptotic homogenization approach. Zhong et al.[19] constructed a micromechanical model based on the variation asymptotic homogenization method, and obtained local stress field and magnetic flux density. Based on Eshelby equivalent inclusion and Mori Tanaka method, Xue[20] and Guan[21] predicted the effective magnetostrictive strain of particle reinforced composites.

In recent years, a new microscopic model of the finite-volume direct-averaging micromechanics (FVDAM), was proposed by employing the finite volume theory and the boundary conditions of the surface-averaged force and displacement[22,23]. Khatam[24] and Cavalcante[25] further improved the accuracy of the method by introducing parametric elements to discretize the model. Li et al.[26] introduced the mechanical-electrical constitutive relation into the FVDAM to analyze the effective properties and local stress distribution of piezoelectric composites. Ye et al.[27,28] presented an effective FVDAM model for fiber-reinforced composites with initial damages to investigate the local stress distribution and damage evolution at constitutive material level. Cai et al.[29] proposed a novel mechanical property evaluation procedure with consideration of primary pores for random short fiber reinforced composites by constructing a 3D parametric FVDAM model. The homogenized properties and localized field distributions of the magnetostrictive composites[30] were also extensively investigated by using the FVDAM with full consideration of the coupled mechanical-magnetic effects. However, to the best knowledge of the authors, studies on nonlinear characteristics of magnetostrictive composites with coupled mechanical-magnetic effects are not available in the literature.

Based on the microscopic modeling scheme of the FVDAM, this paper presents a coupled nonlinear mechanical-magneto-thermal model at the microscopic scale to study the effective mechanical behaviors of magnetostrictive composites. The outline of the paper is summarized as follows: The coupled nonlinear constitutive equation is given in Section 2. In Section3, the nonlinear microscopic modeling process of magnetostrictive composites subjected to a coupled mechanical-magnetic condition is presented. Their nonlinear equivalent properties are effectively evaluated by the proposed numerical model. In Section 4, comparisons between the results from experiments and the numerical model are presented. Section 5 summarizes the current results.

2. Constitutive relation of magnetostrictive materials

2.1. Thermodynamic constitutive equation

In order to establish a coupled magneto-thermal-mechanical constitutive relation, the equations of thermodynamics in the form of the Gibbs free energy function are employed. The differential expression of the internal energy function U is written as the function of magnetization vectors M_k and entropy density S, that is,

$$dU(\varepsilon_{ij}, M_k, S) = \sigma_{ij} d\varepsilon_{ij} + \mu_0 H_k dM_k + TdS \tag{1}$$

where σ_{ij} and ε_{ij} are the stress and strain components, respectively. H_k and T are the magnetic field intensity and temperature, respectively. S is the entropy density. The subscripts i, j, k represent the direction of the vector components in the three-dimensional Cartesian coordinate system x_1-x_2-x_3 as shown in Fig. 1(a). $\mu_0 = 4\pi \times 10^{-7}$ H/m is the vacuum permeability. The Gibbs free energy density function G of the magnetostrictive materials is defined as:

$$G(\sigma_{ij}, M_k, T) = U - TS - \sigma_{ij}\varepsilon_{ij} \tag{2}$$

The thermodynamic relations are written as:

$$\varepsilon_{ij} = \frac{\partial G(\sigma_{ij}, M_k, T)}{\partial \sigma_{ij}}, \ \mu_0 H_k = \frac{\partial G(\sigma_{ij}, M_k, T)}{\partial M_k} \text{ and } S = -\frac{\partial G}{\partial T} \tag{3}$$

To obtain the constitutive relations in the form of polynomials, Jin[31] expressed the Gibbs free energy in a Taylor series expansion of stresses and magnetization at a reference point $(\sigma_{ij}, M_k) = (0,0)$, and proposed the following general constitutive equations for nonlinear magnetostrictive materials.

$$\varepsilon_{ij} = \varepsilon_{ij}^{(0)}(\sigma_{mn}, \Delta T) + \varepsilon_{ij}^{(1)}(\sigma_{mn}, \Delta T, M_k) \tag{4a}$$

$$H_k = H_k^{(0)}(M_l, \Delta T) + H_k^{(1)}(M_l, \Delta T, \sigma_{mn}) \tag{4b}$$

where $\Delta T = T - T_0$ is the change of temperature. T and T_0 are the ambient temperature and the reference temperature, respectively. $\varepsilon_{ij}^{(0)}(\sigma_{mn}, \Delta T)$ includes both elastic and thermal expansion strain that are independent of the magnetic field. $\varepsilon_{ij}^{(1)}(\sigma_{mn}, \Delta T, M_k)$ is the magnetization-dependent magnetostrictive strain. $H_k^{(0)}(M_l, \Delta T)$ represents the free state magnetic field intensity ($\sigma_{mn} = 0$), and $H_k^{(1)}(M_l, \Delta T, \sigma_{mn})$ is the magnetic field intensity when the material is stressed. The strain component ε_{ij} in the constitutive relation is further expressed as:

$$\varepsilon_{ij} = \frac{1}{E}\left[(1+v)\sigma_{ij} - v\sigma_{kk}\delta_{ij}\right] + \bar{\alpha}\Delta T\delta_{ij} + \frac{\lambda_s}{\sigma_s}\left(\frac{3}{2}\sigma_{ij} - \frac{1}{2}\sigma_{kk}\delta_{ij}\right) +$$

$$\frac{1}{M_s^2}\left\{\frac{3}{2}\lambda_s M_i M_j - M_k M_k\left[\frac{\lambda_s}{2}\delta_{ij} - \bar{\beta}\Delta T\delta_{ij} + \frac{\lambda_S\left(\frac{3}{2}\sigma_{ij} - \frac{1}{2}\sigma_{kk}\delta_{ij}\right)}{\sigma_s}\right]\right\} \qquad (5)$$

where E and v are the Young's modulus and Poisson's ratio, respectively. $\bar{\alpha}$ and $\bar{\beta}$ are the thermal expansion coefficients and thermal expansion coefficients at magnetization saturation, respectively. λ_s, M_s and σ_s are the saturation magnetostrictive strain, saturation magnetization and maximum pre-stress, respectively. δ_{ij} is the Kronecker delta.

The magnetic field intensity components H_k in equation (4b) can be further expressed as:

$$H_k = \frac{1}{k(T)M}L^{-1}\left(\frac{M}{M_s(T)}\right)M_k - \frac{\lambda_s}{\mu_0 M_s^2}\left[3\sigma_{ij} - \sigma_{kk}\delta_{ij} - \left(\frac{3\sigma_{ij}^2 - \sigma_{kk}^2}{2}\right)\frac{\delta_{ij}}{\sigma_s}\right]M_j - \frac{2\bar{\beta}}{\mu_0 M_s^2}\Delta T\sigma_{kk}M_k \qquad (6)$$

where $M = \sqrt{M_1^2 + M_2^2 + M_3^2}$, $L^{-1}(.)$ is the inverse of the Langevin function $L(x) = \coth(x) - 1/x$ and $k(T) = \frac{3\chi_m}{M_S(T)}$ is the relaxation factor with magnetic susceptibility χ_m. The temperature-dependent saturation magnetization $M_s(T)$ is given by,

$$M_s(T) = M_s\left(\frac{1 - T/T_c}{1 - T_0/T}\right)^{1/2} \qquad (7)$$

where T_c is the Curie temperature.

2.2. Coupled mechanical-magnetic-thermal constitutive model

With consideration of nonlinear properties of a magnetostrictive material, an incremental approach is followed to describe the relationship between the mechanical and the magnetic responses. At each increment step, a linear relation in the form of the generalized Hooke's law is assumed, as follows:

$$\Delta\sigma_{ij} = C_{ijkl}\Delta\varepsilon_{kl} - q_{ijk}\Delta H_k - \Lambda_{ij}\Delta T$$
$$\Delta B_i = q_{ikl}\Delta\varepsilon_{kl} + \mu_{ik}\Delta H_k + m_i\Delta T \qquad (8)$$

where $\Delta\sigma_{ij}$ and ΔB_i are, respectively, stress increment and flux density increment. C_{ijkl}, q_{ijk}, Λ_{ij}, μ_{ik} and m_i denote elastic stiffness coefficient, piezomagnetic coefficient, thermal stress coefficient, magnetic permeability coefficient and pyromagnetic coefficient, respectively. With consideration of the coupled mechanical-magnetic-thermal effects, the generalized magnetic-

mechanical coupling can be written in the following matrix form.

$$\begin{bmatrix} \Delta\boldsymbol{\sigma} \\ \Delta\mathbf{B} \end{bmatrix} = \begin{bmatrix} \mathbf{C} & \mathbf{q}^{\mathbf{T}} \\ \mathbf{q} & \mathbf{-\mu} \end{bmatrix} \begin{bmatrix} \Delta\boldsymbol{\varepsilon} \\ \mathbf{-\Delta H} \end{bmatrix} + \begin{bmatrix} \boldsymbol{\Lambda} \\ \mathbf{m} \end{bmatrix} \Delta T = \mathbf{G} \begin{bmatrix} \Delta\boldsymbol{\varepsilon} \\ \Delta\mathbf{H} \end{bmatrix} + \boldsymbol{\Gamma}\Delta T \tag{9}$$

Where $\quad \Delta\boldsymbol{\sigma} = \begin{bmatrix} \Delta\sigma_{11} & \Delta\sigma_{22} & \Delta\sigma_{33} & \Delta\sigma_{23} & \Delta\sigma_{13} & \Delta\sigma_{12} \end{bmatrix}^{T}$, $\quad \Delta\mathbf{H} = \begin{bmatrix} \Delta H_1 & \Delta H_2 & \Delta H_3 \end{bmatrix}^{T}$,

$\Delta\mathbf{B} = \begin{bmatrix} \Delta B_1 & \Delta B_2 & \Delta B_3 \end{bmatrix}^{T}$, $\quad \Delta\boldsymbol{\varepsilon} = \begin{bmatrix} \Delta\varepsilon_{11} & \Delta\varepsilon_{22} & \Delta\varepsilon_{33} & 2\Delta\varepsilon_{23} & 2\Delta\varepsilon_{13} & 2\Delta\varepsilon_{12} \end{bmatrix}^{T}$. $\mathbf{G}$ and $\boldsymbol{\Gamma}$ are

the 9×9 magneto-elastic coefficient matrix and the 9×1 thermal stress-magnetic coefficient

matrix, which can be expressed, respectively, as:

$$\mathbf{G} = \begin{bmatrix} C_{11} & C_{12} & C_{13} & C_{14} & C_{15} & C_{16} & q_{11} & q_{21} & q_{31} \\ C_{21} & C_{22} & C_{23} & C_{24} & C_{25} & C_{26} & q_{12} & q_{22} & q_{32} \\ C_{31} & C_{32} & C_{33} & C_{34} & C_{35} & C_{36} & q_{13} & q_{23} & q_{33} \\ C_{41} & C_{42} & C_{43} & C_{44} & C_{45} & C_{46} & q_{14} & q_{24} & q_{34} \\ C_{51} & C_{52} & C_{53} & C_{54} & C_{55} & C_{56} & q_{15} & q_{25} & q_{35} \\ C_{61} & C_{62} & C_{63} & C_{64} & C_{65} & C_{66} & q_{16} & q_{26} & q_{36} \\ q_{11} & q_{12} & q_{13} & q_{14} & q_{15} & q_{16} & -\mu_{11} & -\mu_{21} & -\mu_{13} \\ q_{21} & q_{22} & q_{23} & q_{24} & q_{25} & q_{26} & -\mu_{21} & -\mu_{22} & -\mu_{23} \\ q_{31} & q_{32} & q_{33} & q_{34} & q_{35} & q_{36} & -\mu_{31} & -\mu_{32} & -\mu_{33} \end{bmatrix}, \boldsymbol{\Gamma} = \begin{bmatrix} \Lambda_1 \\ \Lambda_2 \\ \Lambda_3 \\ \Lambda_4 \\ \Lambda_5 \\ \Lambda_6 \\ m_1 \\ m_2 \\ m_3 \end{bmatrix} \tag{10}$$

The linear constitutive equations mentioned above satisfy the stress equilibrium and Maxwell's

equations in the Cartesian coordinates x_i, i.e.,

$$\frac{\partial \sigma_{ij}}{\partial x_j} = 0, \quad \frac{\partial B_i}{\partial x_i} = 0 \tag{11}$$

where B_i are the components of the magnetic flux density which is related to magnetic field

density components H_i and magnetization components M_i in the form $B_i = \mu_0 (H_i + M_i)$.

Solving Eq. (9) and considering Eq. (11) yield

$$\begin{bmatrix} \Delta\boldsymbol{\varepsilon} \\ \Delta\mathbf{H} \end{bmatrix} = \begin{bmatrix} \mathbf{P}_{11} & \mathbf{P}_{12} \\ \dfrac{1}{\mu_0}\mathbf{P}_{12}^{\mathbf{T}} & \mathbf{P}_{22} \end{bmatrix} \begin{bmatrix} \Delta\boldsymbol{\sigma} \\ \Delta\mathbf{M} \end{bmatrix} + \begin{bmatrix} \mathbf{R}_1 \\ \mathbf{R}_2 \end{bmatrix} \Delta T = \mathbf{P} \begin{bmatrix} \Delta\boldsymbol{\sigma} \\ \Delta\mathbf{M} \end{bmatrix} + \mathbf{R}\Delta T \tag{12}$$

where the coefficient matrix $\mathbf{P}$ contains the flexibility coefficients, piezomagnetic coefficients
and permeability components, which can be obtained by differentiating Eqs. (5)-(6) with respect to
σ, M, T, respectively, as follows:

$$\mathbf{P}_{11} = \frac{\partial \varepsilon}{\partial \sigma} = \begin{bmatrix} \mathbf{A} & \mathbf{O}_3 \\ \mathbf{O}_3 & \mathbf{B} \end{bmatrix}, \quad \mathbf{P}_{12} = \frac{\partial H}{\partial \sigma} = \begin{bmatrix} \mathbf{C} \\ \mathbf{O} \end{bmatrix}, \quad \mathbf{P}_{22} = \frac{\partial H}{\partial M} = \mathbf{I}_3\mathbf{D}, \quad \mathbf{R}_1 = \frac{\partial \varepsilon}{\partial T}, \quad \mathbf{R}_2 = \frac{\partial H}{\partial T} \tag{13}$$

where $\mathbf{O}_3$ and $\mathbf{I}_3$ are third-order zero matrix and third-order unit matrix, respectively. The
detailed expressions of $\mathbf{A}$, $\mathbf{B}$, $\mathbf{C}$, $\mathbf{D}$, $\mathbf{R}_1$ and $\mathbf{R}_2$ can be found in Appendix 1. Matrix $\mathbf{Q}$ is
the inverse matrix of $\mathbf{P}$, i.e.,

$$\mathbf{Q} = \mathbf{P}^{-1} = \begin{bmatrix} \mathbf{P}_{11} & \mathbf{P}_{12} \\ \dfrac{1}{\mu_0}\mathbf{P}_{12}^{\mathbf{T}} & \mathbf{P}_{22} \end{bmatrix}^{-1} = \begin{bmatrix} \mathbf{Q}_{11} & \mathbf{Q}_{12} \\ \dfrac{1}{\mu_0}\mathbf{Q}_{12}^{\mathbf{T}} & \mathbf{Q}_{22} \end{bmatrix} \tag{14}$$

From Eq. (9), the linear magneto-elastic coefficient matrix $\mathbf{G}$ can be replaced by a 9×9 nonlinear material matrix $\mathbf{Q}$, that is,

$$\begin{bmatrix} \Delta\boldsymbol{\sigma} \\ \Delta\mathbf{B} \end{bmatrix} = \begin{bmatrix} \mathbf{Q}_{11} & -\mathbf{Q}_{12} \\ -\mathbf{Q}_{12}^{\mathbf{T}} & -\mu_0(\mathbf{Q}_{22}+\mathbf{I}_3) \end{bmatrix}\begin{bmatrix} \Delta\boldsymbol{\varepsilon} \\ -\Delta\mathbf{H} \end{bmatrix} - \begin{bmatrix} \mathbf{Q}_{11}\boldsymbol{\Lambda}+\mathbf{Q}_{12}\mathbf{m} \\ -\mathbf{Q}_{12}^{\mathbf{T}}\boldsymbol{\Lambda}+\mu_0\mathbf{Q}_{22}\mathbf{m} \end{bmatrix}\Delta T \tag{15}$$

Eq. (15) can be further expressed in a more compact matrix form:

$$\Delta\mathbf{Y} = \mathbf{Q}\Delta\mathbf{X} - \boldsymbol{\Phi}\Delta T \tag{16}$$

where
$$\begin{aligned}
\Delta\mathbf{Y} &= \begin{bmatrix} \Delta\sigma_{11} & \Delta\sigma_{22} & \Delta\sigma_{33} & \Delta\sigma_{23} & \Delta\sigma_{12} & \Delta\sigma_{13} & \Delta B_1 & \Delta B_2 & \Delta B_3 \end{bmatrix}^T \\
\Delta\mathbf{X} &= \begin{bmatrix} \Delta\varepsilon_{11} & \Delta\varepsilon_{22} & \Delta\varepsilon_{33} & \Delta\varepsilon_{23} & \Delta\varepsilon_{12} & \Delta\varepsilon_{13} & \Delta H_1 & \Delta H_2 & \Delta H_3 \end{bmatrix}^T
\end{aligned}$$

3. Microscopic mechanical model

The effective property of the magnetostrictive composite[13] is dependent closely on the volume fraction of inclusion and microstructure characteristics, etc. To simplify the modeling procedure, it is assumed that the continuous fibers are periodically distributed in the matrix, as shown in Fig. 1(a), where the macroscopic structure is presented in the three-dimensional coordinate system, $x_1 - x_2 - x_3$. A representative volume element (RVE), as shown in Fig.1(b), is chosen to represent the composite. Since this can be approximately considered as a plane strain problem, the stress and strain of the continuous fiber-reinforced composites in the x_1−direction are assumed to be constant along the direction of the fibers. Thus, the axial strain of the sub-cells is equal to the macroscopic axial strain, that is $\varepsilon_{11}^{(q)} = \bar{\varepsilon}_{11}$. The RVE is further discretized by 48×48 parametric sub-cells in the $x_2 - x_3$ plane, as shown in Fig. 1(b).
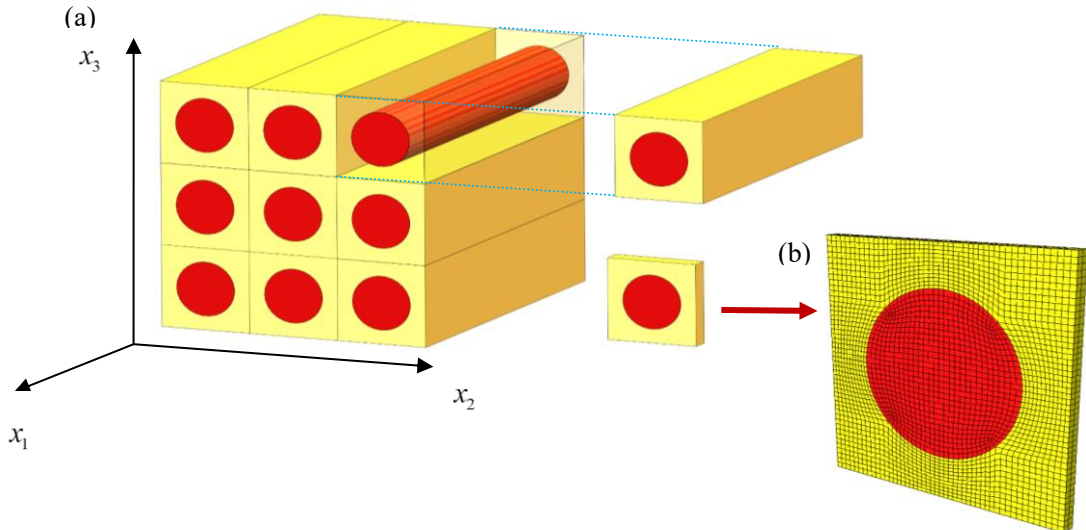

Fig. 1. Schematic diagrams of the periodic structure and parametric mesh in continuous fiber magnetostrictive composites: (a) Periodical arrangement fibers, (b) Parametric RVE.
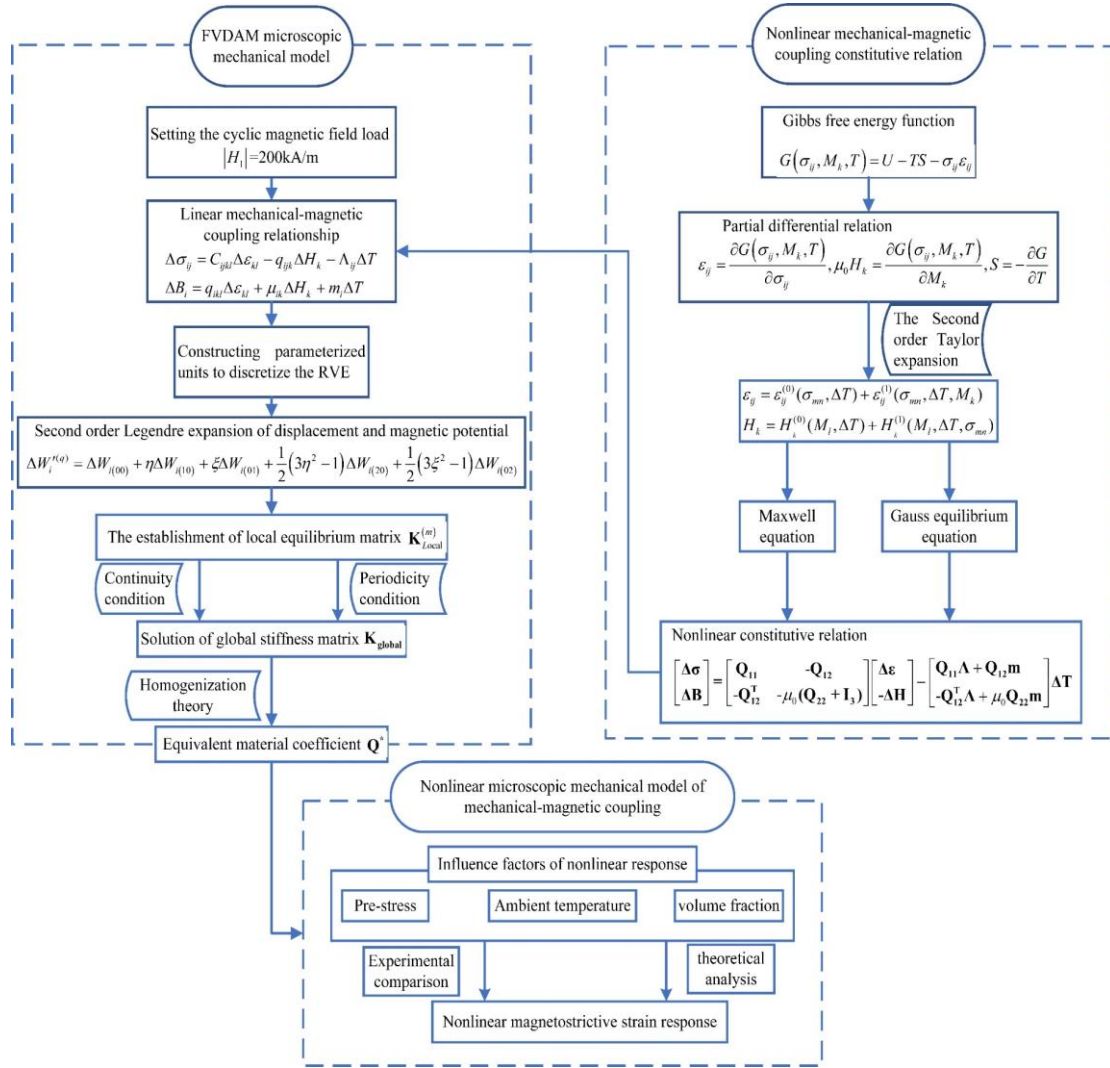
Fig. 2. The nonlinear modeling process of the magnetostrictive composites under mechanical-magnetic coupling condition

The coupled mechanical-magnetic-thermal nonlinear modeling process is illustrated by the flowchart shown in Fig. 2, which involves the following five steps:

(a)The Gibbs free energy density function $G\left(\sigma_{ij}, M_k, T\right) = U - TS - \sigma_{ij}\varepsilon_{ij}$ is firstly established, and the differential relation of the stress components σ_{ij}, magnetization vectors M_k and temperature T is obtained in Eq. (3). The nonlinear general constitutive relation of the magnetostrictive materials is obtained by the second-order Taylor expansion. The constitutive equation is expressed in an incremental form at each incremental step due to its nonlinearity in Eq. (8). Moreover, the Maxwell equation and the Gauss equilibrium equation are used to obtain the nonlinear mechanical-magnetic coupling coefficient matrix $\mathbf{Q}$.

(b)The magnetic field load is applied. The tangential strain increment $\Delta\varepsilon_{ij}$ and the magnetic

field intensity increment ΔH_i are calculated for the stress vector equation and the magnetic flux density vector equation with consideration of the nonlinear relationship in Eq. (16).

(c)Parametric elements are constructed to discretize the RVE. The local displacement $\Delta u_i^{(q)}$ and the magnetic potential $\Delta \phi^{(q)}$ of each sub-cell are expanded by a second-order Legendre polynomial. The local stiffness coefficient matrix $\mathbf{K}_{\mathbf{Local}}^{(q)}$ is obtained by considering local equilibrium.

(d)The global stiffness equation is solved after imposing the periodic and continuity conditions between adjacent sub-cells. The strain components $\overline{\mathbf{\varepsilon}}^{(\beta,\gamma)} = \mathbf{A}^{(q)}\overline{\mathbf{\varepsilon}} + \mathbf{D}^{(q)}$ of each sub-cell are obtained by constructing the Hill strain matrix $\mathbf{A}^{(q)}$. Based on the homogenization theory, the equivalent material coefficient $\mathbf{Q}^*$ is obtained as weighted average of the material coefficient of each sub-cell, and can be expressed as $\mathbf{Q}^* = \dfrac{1}{S}\displaystyle\sum_{\gamma=1}^{N_\gamma}\sum_{\beta=1}^{N_\beta} L_\beta L_\gamma \mathbf{Q}^{(\beta,\gamma)}\mathbf{A}^{(\beta,\gamma)}$.

3.1. Parametric meshing

The $N_\beta \times N_\gamma$ parametric meshes shown in Fig. 3(a) are used to discretize the section, which are particularly suitable for the curved interface and improve the accuracy of the model. The general quadrilateral elements in coordinates (y_2, y_3) are the mapping of the square elements in the reference coordinates (ξ, η). The actual position coordinates of the qth sub-cell is $\left(y_2^{(m,q)}, y_3^{(m,q)}\right)$ as seen in Fig. 3(b). The four sides of the sub-cell are denoted by F_m numbered clock-wisely. Thus, the normal of the sides are $n^{(m,q)} = \left(n_2^{(m,q)}, n_3^{(m,q)}\right)$ and can be written as:

$$n_2^{(m,q)} = \frac{y_3^{(m+1,q)} - y_3^{(m,q)}}{l_m}, \quad n_3^{(m,q)} = \frac{y_2^{(m+1,q)} - y_2^{(m,q)}}{l_m} \tag{17}$$

where $L_m = \sqrt{\left(y_2^{(m+1,q)} - y_2^{(m,q)}\right)^2 + \left(y_3^{(m+1,q)} - y_3^{(m,q)}\right)^2}$ is the boundary length of the quadrilateral cell. Note that when $m+1=5$, the position co-ordinates are identical to those when $m=1$.

The parametric elements are constructed in the reference coordinate system $\eta - \xi$, wherein the plane bounds of $-1 \le \eta \le 1$ and $-1 \le \xi \le 1$ are satisfied. The shape functions $N_m(\eta, \xi)$ are used to characterize the mapping relation between the coordinate system and the reference coordinate system. For the qth sub-cell, the vertices $y_i^{(q)}(\eta, \xi)$ in the reference coordinate system can be

transformed from the vertices $y_i^{(m,q)}$ in the origin all coordinate system, given by,

$$y_i^{(q)}(\eta,\xi) = \sum_{m=1}^{4} N_m(\eta,\xi) y_i^{(m,q)} \tag{18}$$

where
$$N_1 = \frac{1}{4}(1-\xi)(1-\eta) \qquad N_2 = \frac{1}{4}(1-\xi)(1+\eta)$$
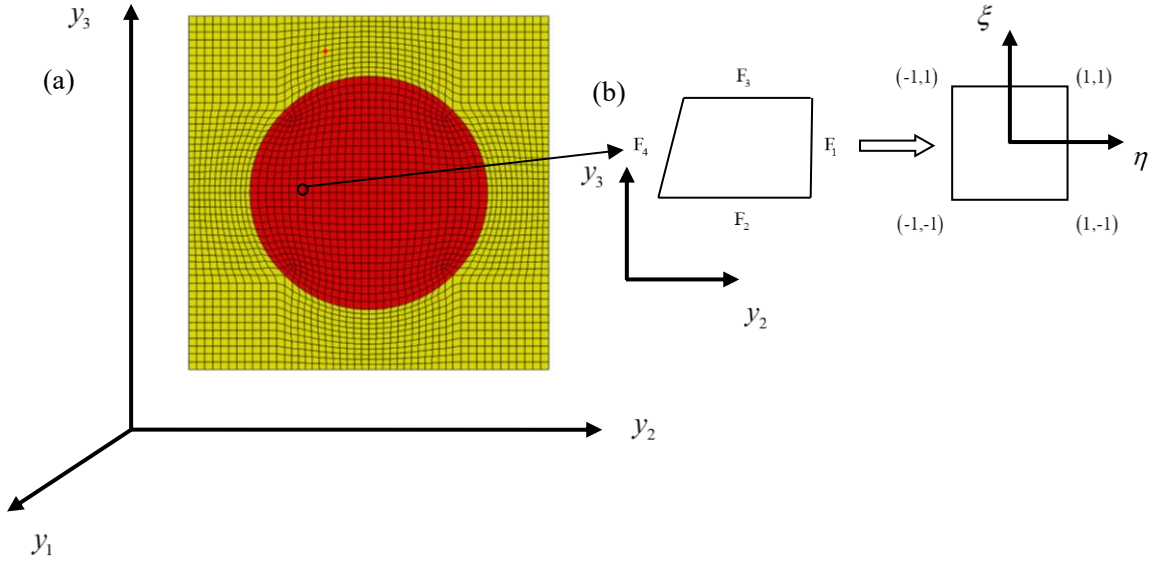$$N_3 = \frac{1}{4}(1+\xi)(1+\eta) \qquad N_4 = \frac{1}{4}(1+\xi)(1-\eta)$$

Fig. 3. Mapping relation during the parametric modeling (a) Parameterized mesh, (b) Mapping relation.

3.2. Construction of the local stiffness matrix

According to the homogenization theory[32], the incremental forms of the displacement components $\Delta u_i^{(q)}$ and magnetic potential $\Delta\phi^{(q)}$ for the qth sub-cell can be represented by a two-scale expansion involving the macroscopic and the fluctuating components, that is,

$$\Delta u_i^{(q)} = \Delta\overline{\varepsilon}_{ij} x_j + \Delta u_i'^{(q)}$$
$$\Delta\phi^{(q)} = -\Delta\overline{H}_j x_j + \Delta\phi'^{(q)} \tag{19}$$

where $\Delta\overline{\varepsilon}_{ij}$ and $\Delta\overline{H}_j$ are increments of the average macroscopic strain and the average magnetic field intensity, respectively. The fluctuating displacements $\Delta u_i'^{(q)}$ and the magnetic potential components $\Delta\phi'^{(q)}$ can be further expanded into a second-order Legendre expansion in the reference coordinate system $(\eta,\xi)^q$, as follows,

$$\Delta W_i''^{(q)} = \Delta W_{i(00)} + \eta \Delta W_{i(10)} + \xi \Delta W_{i(01)} + \frac{1}{2}\left(3\eta^2 - 1\right)\Delta W_{i(20)} + \frac{1}{2}\left(3\xi^2 - 1\right)\Delta W_{i(02)} \qquad (20)$$

where $\Delta W_i'^{(q)} = \begin{bmatrix} \Delta u_1'^{(q)} & \Delta u_2'^{(q)} & \Delta u_3'^{(q)} & \Delta \phi'^{(q)} \end{bmatrix}$. The unknown coefficients $\Delta W_{i(mn)}^{(q)} (i = 1,2,3,4)$ are intermediate variables, which are determined by satisfying the sub-cell interfacial continuity conditions, the periodical conditions and the local equilibrium equations. The coefficients $\Delta W_{i(mn)}^{(q)}$ are related to the sub-cell interface displacements and sub-cell generalized plane displacements.

The intermediate variables related to the internal magnetic potential and surface-averaged magnetic potential are the unknown parameters in the parametric FVDAM model. For the qth sub-cell in the reference coordinate system, the fluctuating surface-averaged displacements and magnetic potentials on faces $F_1, F_3 (\xi = \mp 1)$ and $F_2, F_4 (\eta = \pm 1)$ can be calculated by integrating the respective interfacial displacements and magnetic potentials, that is,

$$\Delta W_i''^{(1,3)} = \frac{1}{2}\int_{-1}^{+1} \Delta W_i'(\eta, \mp 1) d\eta = \Delta W_{i(00)} \mp \Delta W_{i(01)} + \Delta W_{i(02)}$$

$$\Delta W_i''^{(2,4)} = \frac{1}{2}\int_{-1}^{+1} \Delta W_i'(\xi, \pm 1) d\xi = \Delta W_{i(00)} \pm \Delta W_{i(10)} + \Delta W_{i(20)} \qquad (21)$$

To further reduce the number of the unknown variables, the first-order and second-order coefficients are replaced by the zero-order coefficients. On this basis, the fluctuating displacement and magnetic potential components can be written in a matrix form as:

$$\begin{bmatrix} \Delta W_{i(10)} \\ \Delta W_{i(01)} \\ \Delta W_{i(20)} \\ \Delta W_{i(02)} \end{bmatrix} = \frac{1}{2}\begin{bmatrix} 0 & 1 & 0 & -1 \\ -1 & 0 & 1 & 0 \\ 0 & 1 & 0 & 1 \\ 1 & 0 & 1 & 0 \end{bmatrix}\begin{bmatrix} \Delta \hat{W}_i''^{(1)} - \Delta W_{i(00)} \\ \Delta \hat{W}_i''^{(2)} - \Delta W_{i(00)} \\ \Delta \hat{W}_i''^{(3)} - \Delta W_{i(00)} \\ \Delta \hat{W}_i''^{(4)} - \Delta W_{i(00)} \end{bmatrix} \qquad (22)$$

In addition, the local strain and magnetic field intensity can be obtained by employing the fluctuating strain and macroscopic magnetic field intensity components, that is,

$$\Delta \varepsilon_{ij}^{(q)} = \Delta \bar{\varepsilon}_{ij} + \frac{1}{2}\left(\frac{\partial u_i'}{\partial y_j} + \frac{\partial u_j'}{\partial y_i}\right)^{(q)}, \Delta H_i^{(q)} = \Delta \overline{H}_i - \frac{\partial \phi'^{(q)}}{\partial y_i} \qquad (23)$$

The conversion from the actual coordinate system to the isoparametric coordinate system requires partial derivation of the surface-averaged strain and magnetic potential by means of the Jacobian matrix $\mathbf{J}$, that is,

$$\begin{bmatrix} \dfrac{\partial u_i'}{\partial y_2} \\ \dfrac{\partial u_i'}{\partial y_3} \end{bmatrix}^{(q)} = \mathbf{J}^{-1}\begin{bmatrix} \dfrac{\partial u_i'}{\partial \xi} \\ \dfrac{\partial u_i'}{\partial \eta} \end{bmatrix}^{(q)}, \begin{bmatrix} \dfrac{\partial \alpha'}{\partial y_2} \\ \dfrac{\partial \alpha'}{\partial y_3} \end{bmatrix}^{(q)} = \mathbf{J}^{-1}\begin{bmatrix} \dfrac{\partial \alpha'}{\partial \xi} \\ \dfrac{\partial \alpha_i'}{\partial \eta} \end{bmatrix}^{(q)} \qquad (24)$$

where

$$\mathbf{J} = \begin{bmatrix} \dfrac{\partial y_2}{\partial \xi} & \dfrac{\partial y_3}{\partial \xi} \\ \dfrac{\partial y_2}{\partial \eta} & \dfrac{\partial y_3}{\partial \eta} \end{bmatrix} = \begin{bmatrix} \displaystyle\sum_{m=1}^{4} \dfrac{\partial N_m}{\partial \xi} y_2^{(m)} & \displaystyle\sum_{m=1}^{4} \dfrac{\partial N_m}{\partial \xi} y_3^{(m)} \\ \displaystyle\sum_{m=1}^{4} \dfrac{\partial N_m}{\partial \eta} y_2^{(m)} & \displaystyle\sum_{m=1}^{4} \dfrac{\partial N_m}{\partial \eta} y_3^{(m)} \end{bmatrix}, \mathbf{J}^{-1} = \dfrac{1}{|\mathbf{J}|} \begin{bmatrix} A_1 & -A_3 \\ -A_4 & A_6 \end{bmatrix} = \begin{bmatrix} J_{22} & J_{23} \\ J_{32} & J_{33} \end{bmatrix} \tag{25}$$

After the coordinate transformation using the inverse of Jacobian matrix $\mathbf{J}^{-1}$, the fluctuating displacements $\Delta u_i'$ and the magnetic potential components $\Delta \phi'$ in Eq. (20) are substituted into Eq. (23) to obtain the partial derivatives, respectively. The relevant derivatives with respective to the local coordinates are applied to obtain the strain components $\Delta \varepsilon_{ij}^{(m)}$ and the magnetic field intensity $\Delta H_i^{(m)}$ ($m = 1,2,3,4$) for each sub-cell, given by,

$$\Delta \mathbf{X}^{(1,3)} = \Delta \bar{\mathbf{X}}^{(1,3)} + \mathbf{E}_1 \mathbf{W}_1 \mathbf{J}_1$$

$$\Delta \mathbf{X}^{(2,4)} = \Delta \bar{\mathbf{X}}^{(2,4)} + \mathbf{E}_2 \mathbf{W}_2 \mathbf{J}_2 \tag{26}$$

where $\Delta \mathbf{X}$ is the increment of the strain and magnetic field intensity in Eq. (16). $\mathbf{W}_1$ and $\mathbf{W}_2$ are the vectors related to the intermediate differential variables $\Delta W_{i(mn)}^{(q)}$. $\mathbf{J}_1$ and $\mathbf{J}_2$ are related to the elements in $\mathbf{J}^{-1}$. The detailed expressions of $\mathbf{E}_1$ and $\mathbf{E}_2$ can be found in Appendix 2.

In order to investigate the sub-cell interactions, the increments of the surface-averaged traction $\Delta \hat{\mathbf{t}}_i$ and the normal magnetic displacement $\Delta \hat{\boldsymbol{\varphi}}$ are expressed by the boundary stresses $\Delta \sigma_{ji}^{(m)}$ and the internal magnetic flux density $\Delta B_j^{(m)}$, respectively. The integral of the traction $\Delta \mathbf{t}_i$ and the magnetic potential $\Delta \boldsymbol{\varphi}$ over each side of F_m can be obtained:

$$\Delta \hat{\mathbf{t}}_i = \frac{1}{l_m} \int_{-1}^{+1} \Delta \mathbf{t}_i dl = \frac{1}{l_m} \int_{-1}^{+1} \Delta \sigma_{ji}^{(m)} \cdot \mathrm{n}_j^{(m)} dl , \Delta \hat{\boldsymbol{\varphi}} = \frac{1}{l_m} \int_{-1}^{+1} \Delta \boldsymbol{\varphi} dl = \frac{1}{l_m} \int_{-1}^{+1} \Delta B_j^{(m)} \cdot \mathrm{n}_j^{(m)} dl \tag{27}$$

where $\Delta \mathbf{t}_i = \begin{bmatrix} \Delta t_1 & \Delta t_2 & \Delta t_3 \end{bmatrix}^{(m)}$ are the surface-averaged tractions. The average surface displacement and magnetic displacement can be expressed in the matrix form below,

$$\mathbf{I}^{(m)} = \begin{bmatrix} 0 & 0 & 0 & 0 & n_3 & n_2 & 0 & 0 & 0 \\ 0 & n_2 & 0 & n_3 & 0 & 0 & 0 & 0 & 0 \\ 0 & 0 & n_3 & n_2 & 0 & 0 & 0 & 0 & 0 \\ 0 & 0 & 0 & 0 & 0 & 0 & 0 & n_2 & n_3 \end{bmatrix}^{(m)} \quad \Delta \mathbf{Y}^{(m)} = \mathbf{N}^{(m)} \Delta \mathbf{Y}^{(m)} \tag{28}$$

where $\mathbf{I}^{(m)} = \begin{bmatrix} \Delta \hat{t}_1 & \Delta \hat{t}_2 & \Delta \hat{t}_3 & \Delta \hat{\varphi} \end{bmatrix}^{(m)}$. $\mathbf{N}^{(m)}$ contain the normal vector of the sub-cell boundary. $\Delta \mathbf{Y}$ is the increment of stress and magnetic flux intensity in Eq. (16). By averaging the increments of the equilibrium equation and the Maxwell equation in Eq. (11), respectively, the surface-averaged

traction and magnetic displacement are written as:

$$\int_S \Delta\sigma_{ji} \cdot n_j dS = \int_S \Delta\hat{\mathbf{t}}_i dS = \sum_{m=1}^{4} \int_{l_m} \Delta\hat{t}_i^{(m)} dl_m = \sum_{m=1}^{4} l_m \Delta\hat{t}_i^{(m)} = 0$$

$$\int_S \Delta B_i \cdot n_i dS = \int_S \Delta\hat{\boldsymbol{\varphi}} dS = \sum_{m=1}^{4} \int_{l_m} \Delta\hat{\varphi}^{(m)} dl_m = \sum_{m=1}^{4} l_m \Delta\hat{\varphi}^{(m)} = 0$$

(29)

By employing Eq. (22), the zero-order variables $\begin{bmatrix} \Delta W_{1(00)} & \Delta W_{2(00)} & \Delta W_{3(00)} & \Delta W_{4(00)} \end{bmatrix}^{(\beta,\gamma)}$ are used to replace the first-order and second-order intermediate variables. Moreover, the differentials of the intermediate zero-order variables are eliminated by considering the local equilibrium equation (Eq. 29). The relationship between the surface-averaged traction and the normal magnetic displacements can be obtained by Eq. (30), where $\mathbf{Q}$ is the nonlinear material constitutive matrix obtained in Section 2.

$$\mathbf{I}^{(m)} = \mathbf{N}^{(m)} \mathbf{Q}^{(m)} \Delta\bar{\mathbf{X}} + \mathbf{K}_{Local}^{(m)} \mathbf{U}^{(m)} + \boldsymbol{\Gamma}\Delta T$$

(30)

where $\mathbf{U}^{(m)} = \begin{bmatrix} \Delta u_1^{(\beta,\gamma)} & \Delta u_2^{(\beta,\gamma)} & \Delta u_3^{(\beta,\gamma)} & \Delta\phi^{(\beta,\gamma)} \end{bmatrix}$. $\mathbf{K}_{Local}^{(m)}$ is dependent on the geometry of the sub-cell and the nonlinear material coefficients, which can be explicitly expressed as a matrix with 4×4 sub-matrices.

$$\mathbf{K}_{Local}^{(m)} = \begin{bmatrix} K_{11} & K_{12} & K_{13} & K_{14} \\ K_{21} & K_{22} & K_{23} & K_{24} \\ K_{31} & K_{32} & K_{33} & K_{34} \\ K_{41} & K_{42} & K_{43} & K_{44} \end{bmatrix}^{(m)}$$

(31)

3.3. Construction of the global stiffness matrix

The surface-averaged displacements and magnetic potentials are obtained by employing the local stiffness matrix of each sub-cell. On this basis, the global stiffness matrix related to the sub-cell displacements and magnetic potentials can be constructed after imposing the continuity and periodicity conditions of the RVE. The surface-averaged traction and the normal magnetic displacements are continuous across the interfaces between adjacent sub-cells and are expressed as follows:

$$\mathbf{I}^{2(\beta+1,\gamma)} + \mathbf{I}^{4(\beta,\gamma)} = 0 \quad \mathbf{I}^{1(\beta+1,\gamma)} + \mathbf{I}^{3(\beta,\gamma)} = 0$$

(32)

Similarly, the surface-averaged displacements and magnetic potentials of the adjacent sub-cells are written as follows:

$$\mathbf{U}^{2(\beta+1,\gamma)} = \mathbf{U}^{4(\beta,\gamma)} \quad \mathbf{U}^{1(\beta+1,\gamma)} = \mathbf{U}^{3(\beta,\gamma)}$$

(33)

According to the periodic boundary conditions of the RVE, the boundary conditions of the average surface displacement, magnetic potential increment, average surface traction and normal magnetic flux density are written as:

$$\mathbf{I}_i^{2(1,\gamma)} + \mathbf{I}_i^{2(N_\beta+1,\gamma)} = 0 \qquad \mathbf{I}_i^{3(\beta,1)} + \mathbf{I}_i^{3(\beta,N_\gamma+1)} = 0$$

$$\mathbf{U}_i^{2(1,\gamma)} = \mathbf{U}_i^{2(N_\beta+1,\gamma)} \qquad \mathbf{U}_i^{3(\beta,1)} = \mathbf{U}_i^{3(\beta,N_\gamma+1)}$$

(34)

The global stiffness equation of the RVE is written as follows:

$$\mathbf{K}_{\text{global}}\hat{\mathbf{I}} = \Delta\mathbf{C}\Delta\bar{\mathbf{X}}$$

(35)

where $\hat{\mathbf{I}}$ contains all the sub-cell displacements and magnetic potential components. The global stiffness matrix $\mathbf{K}_{\text{global}}$ is an assembly of the local stiffness matrices. The global matrix $\Delta\mathbf{C}$ is the difference of the nonlinear material coefficients between adjacent sub-cells. After the unknown variables $\Delta W_{i(mn)}^{(q)}$ of each sub-cells are solved, the displacements, magnetic potentials, strains, and magnetic field intensities of each sub-cells can be obtained subsequently.

3.4. Homogenization process

The average strain and magnetic field intensity of sub-cell with coordinates (β, γ) are related to the macroscopic strain and magnetic field intensity of the RVE. The local $\Delta\mathbf{X}$ of the sub-cell can be obtained by using the Hill strain concentration matrix $\mathbf{A}^{(\beta,\gamma)}$ [33], that is,

$$\Delta\bar{\mathbf{X}}^{(\beta,\gamma)} = \mathbf{A}^{(\beta,\gamma)}\Delta\bar{\mathbf{X}} + \mathbf{A}^{th(\beta,\gamma)}\Delta T$$

(36)

where $\mathbf{A}^{(\beta,\gamma)}$ are determined from average strain $\Delta\bar{\varepsilon}_{ij}^{(\beta,\gamma)}$ and magnetic field $\Delta\bar{H}_{ij}^{(\beta,\gamma)}$ of the sub-cell. $\mathbf{A}^{th(\beta,\gamma)}$ is the thermal contribution of the sub-cell.

Subsequently, the increments of stress and magnetic flux density can be expressed as the weighted sum of the sub-cell average stress and magnetic displacement, that is,

$$\Delta\hat{\boldsymbol{\sigma}} = \frac{1}{S}\int\Delta\boldsymbol{\sigma}dS = \frac{1}{S}\sum_{\gamma=1}^{N_\gamma}\sum_{\beta=1}^{N_\beta}\int_{S_{(\beta,\gamma)}}\Delta\boldsymbol{\sigma}^{(\beta,\gamma)}dS^{(\beta,\gamma)} = \sum_{\gamma=1}^{N_\gamma}\sum_{\beta=1}^{N_\beta}S^{(\beta,\gamma)}\Delta\boldsymbol{\sigma}^{(\beta,\gamma)}$$

$$\Delta\hat{\mathbf{B}} = \frac{1}{S}\int\Delta\mathbf{B}dS = \frac{1}{S}\sum_{\gamma=1}^{N_\gamma}\sum_{\beta=1}^{N_\beta}\int_{S_{(\beta,\gamma)}}\Delta\mathbf{B}^{(\beta,\gamma)}dS^{(\beta,\gamma)} = \sum_{\gamma=1}^{N_\gamma}\sum_{\beta=1}^{N_\beta}S^{(\beta,\gamma)}\Delta\mathbf{B}^{(\beta,\gamma)}$$

(37)

where $S^{(\beta,\gamma)}$ is the area of the sub-cell.

Substituting the equivalent material coefficients into the nonlinear incremental constitutive relation in Eq. (16), the macroscopic nonlinear incremental constitutive equation of the magnetostrictive composite is found as,

$$\Delta\mathbf{Y} = \mathbf{Q}^*\Delta\mathbf{X} - \boldsymbol{\Phi}^*\Delta T$$

(38)

where the equivalent magneto-elastic coefficients matrix $\mathbf{Q}^* = \begin{bmatrix} \mathbf{C}^* & \mathbf{q}^* \\ \mathbf{q}^{*\mathbf{T}} & -\boldsymbol{\mu}^* \end{bmatrix}$ is determined by the

sub-cell geometry, constitutive law and magneto-elastic concentration matrix of the material. Substituting Eqs. (36) and (37) into Eq. (38) yields the following nonlinear equivalent material coefficient matrix $\mathbf{Q}^*$.

$$\mathbf{Q}^* = \frac{1}{S} \sum_{\gamma=1}^{N_\gamma} \sum_{\beta=1}^{N_\beta} L_\beta L_\gamma \mathbf{Q}^{(\beta,\gamma)} \mathbf{A}^{(\beta,\gamma)} \tag{39}$$

3.4. Convergence study

To study mesh sensitivity of the model, results from using 48×48 and 96×96 sub-cells are obtained, respectively, and compared in Fig.4 for an axial magnetic field intensity of 20KA/m. The equivalent elastic modulus and the equivalent piezomagnetic coefficients are computed by the numerical model. The fiber volume fraction of the material ranges from 0.05 to 0.70. From the numerical results shown in Fig. 4, it can be seen that the results from the RVEs discretized by 48×48 and 96×96 elements are virtually the same, suggesting that a mesh of 48×48 is suffice for the model to provide accurate predictions with reduced computational costs. Thus, the RVEs in the following calculations are all discretized by 48×48 sub-cells.
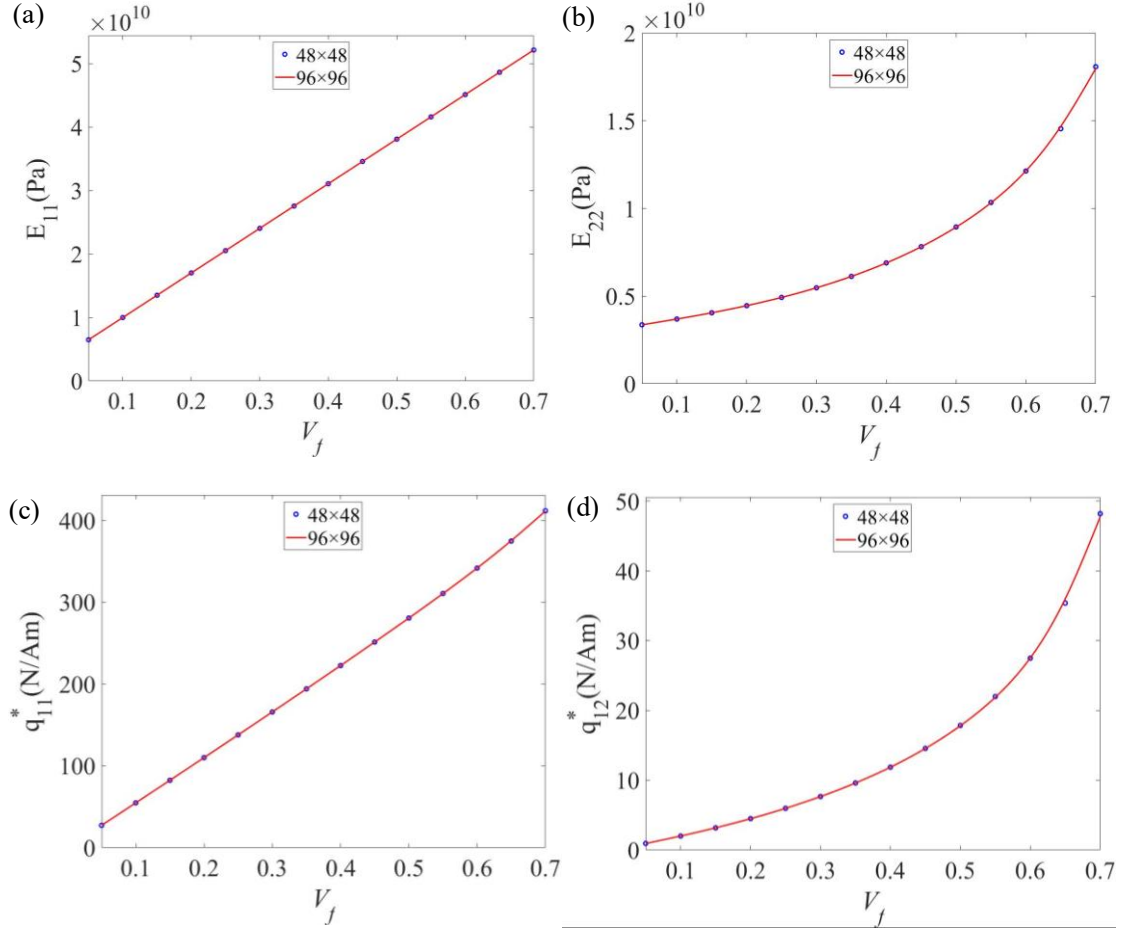

Fig. 4. Convergence investigation of the composites with consideration of sub-cell number (a) E_{11}, (b) E_{22}, (c) q_{11}^* and (d) q_{12}^*.

4. Applications and discussions

In this Section, the effects of magnetic field variation, pre-stress and temperature on the nonlinear properties of Terfenol-D fiber-reinforced epoxy matrix composites are investigated under different loading conditions. The constituent material properties of the fiber and the matrix are given in Table 1 and Table 2, respectively. To study the influence of fiber contents, three different fiber volume fractions (V_f), i.e., 0.35, 0.46 and 0.70, are considered.

Table1. Material parameters of the Terfenol-D fiber [34]

Material properties	Implication	Value
E	Elasticity modulus	$110\,\mathrm{Gpa}$
v	Poisson ratio	0.3
$\bar{\alpha}$	Coefficient of thermal expansion	$12\times10^{-6}\ \mathrm{K}^{-1}$
$\bar{\beta}$	Coefficient of saturation magnetization thermal expansion	$-1.3\times10^{-6}\ \mathrm{K}^{-1}$
T_0	The reference temperature	$293\,\mathrm{K}$
T_c	The Curie temperature	$656.3\,\mathrm{K}$
λ_s	The saturation magnetostriction	1.1×10^{-3}
M_s	The saturation magnetization	$638\,\mathrm{kA/m}$
σ_s	Maximum pre-stress	$200\,\mathrm{Mpa}$
χ_m	The magnetic susceptibility	14

Table 2. Material parameters of the epoxy matrix[34]

Material properties	E (GPa)	v	$\bar{\alpha}\ \left(\mathrm{K}^{-1}\right)$
Epoxy	3	0.35	54×10^{-6}

4.1. A Comparison with the experimental data

The macroscopic axial strain increment $\Delta\varepsilon_{11}$ is plotted against the axial magnetic field intensity H_1 in Fig. 5 for the materials of different fiber volumes when the ambient temperature is the reference temperature $T=T_0$. Comparing with the experimental results[35], it can be found that the current method presents a higher accuracy than the Mori-Tanaka theory when the fiber volume fractions are equal to 0.35 and 0.46, as shown in Figs. 5(a)-(b). It is interesting to mention that the current method predicts a higher level of nonlinearity, especially when the composite has a lower fiber ratio. This may be attributable to the pore defects, which are ignored in the numerical modeling, resulting in a reduction of the nonlinear magnetostrictive strain. In addition, the magnetic susceptibility of the composite may be overestimated by the numerical method without considering the interaction forces, which may lead to a higher nonlinear magnetostrictive effect. It should be

pointed out that the present method agrees very well with the experimental results when the magnetization is close to magnetic saturation ($|H_1|$>100kA/m). Both theoretical methods agree with the experimental data well when the fiber volume fraction is equal to 0.7, as shown in Fig. 5(c). This may be attributed to the increase of the fiber volume fraction. In other words, the mechanical property of the magnetostrictive composites is close to those of a monolithic magnetostrictive material, which results in a good consistency with the experimental results.
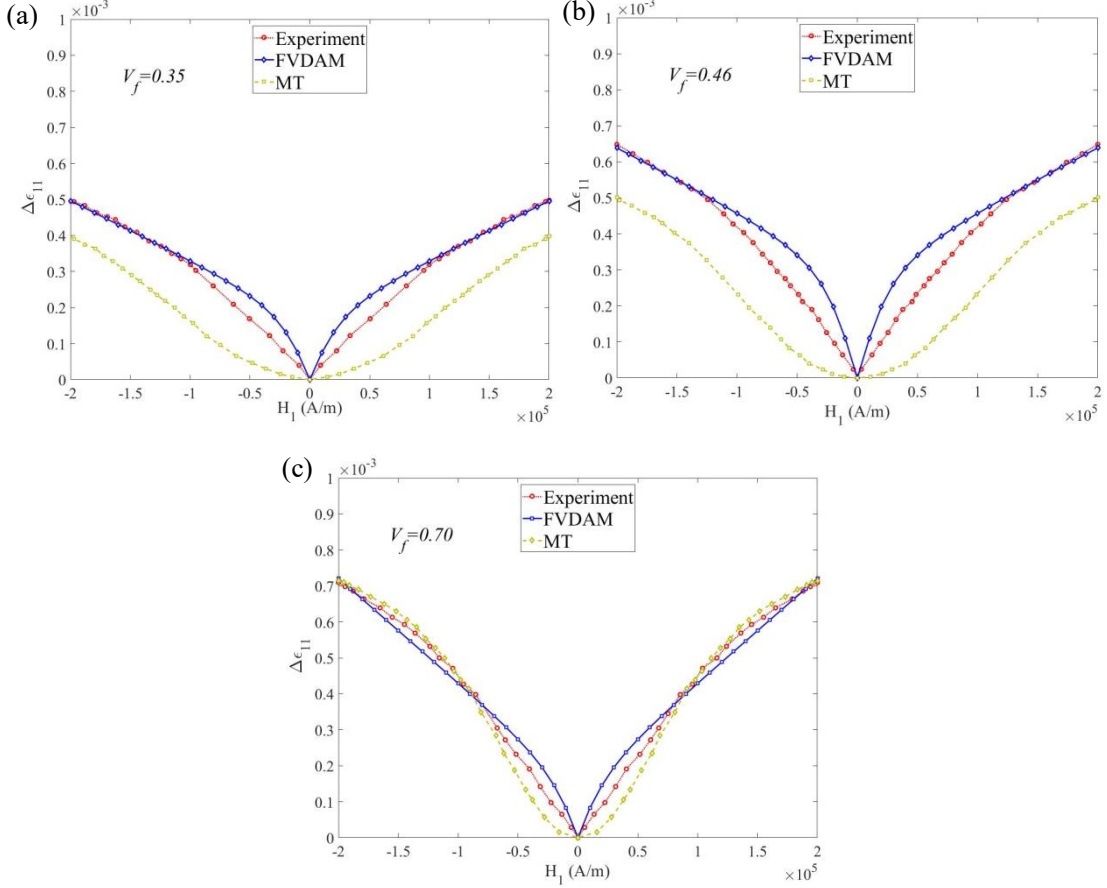
Fig. 5. Validation of the proposed micromechanical model (a) V_f=0.35, (b) V_f=0.46, and (c) V_f=0.70.

4.2. Investigation of nonlinear responses

The influences of average pre-stress on the magnetization effect of the magnetostrictive composites are investigated. Fig. 6 shows the magnetization intensity undergone axial pre-stresses σ_{11} of 1MPa, 8MPa and 16MPa at reference temperature $T=T_0$. The fiber volume fraction is chosen to be 0.35. Clearly, the magnetization process exhibits a slow growth when $|H_1|$>60kA/m. This is because the magnetic domain and the magnetic domain walls are no longer offset by the magnetic fields, which can be explained by the relationship between the magnetization and magnetic fields in Eq. (6). In addition, it can be seen that in general the increase of the pre-stress increases magnetization intensity $\mu_0 M_1$, while has little effect on the maximum amplitude of the

magnetization intensity, $\mu_0 = 4\pi \times 10^{-7} \text{H/m}$ is the vacuum permeability. The maximum

magnetization intensity $\mu_0 M_1^{\max}$ eventually reaches 0.74T, which is determined by the property

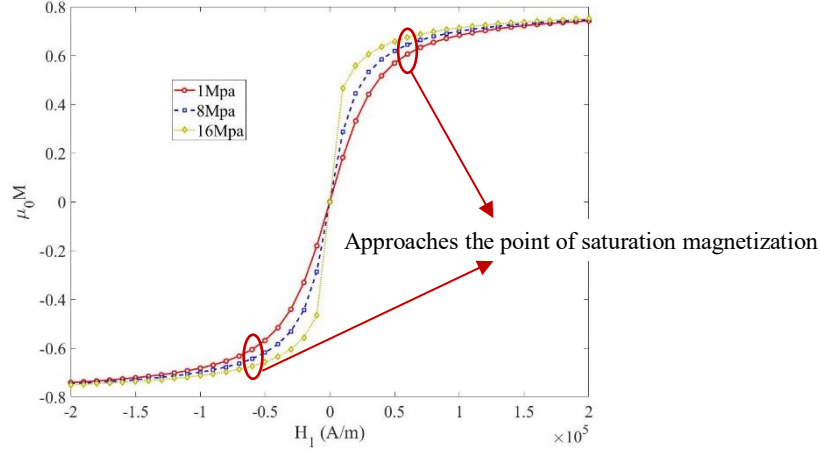of the magnetostrictive material.

Fig. 6. The influences of pre-stress $\bar{\sigma}_{11}$ on magnetization effects

Fig. 7 shows the magnetization process with respect to macroscopic strain and magnetic flux

density at the reference temperature $T = T_0$. Three different axial pre-stresses, i.e., 1MPa, 8MPa

and 16MPa are considered. Similarly, the axial strain $\bar{\varepsilon}_{11}$ and the magnetic flux density $\bar{B}_1$ exhibit

strong nonlinear property when the absolute value of magnetic field intensity $|H_1| < 60\text{kA/m}$.

Moreover, the pre-stress tends to increase the amplitude of the total axial strain $\bar{\varepsilon}_{11}$ and the

magnetic flux density $\bar{B}_1$. Similarly, the axial strain $\bar{\varepsilon}_{11}$ and the magnetic flux density $\bar{B}_1$

increase almost linearly with the magnetic field intensity when $|H_1| \geq 60\text{kA/m}$ and the material is

in the state of magnetic saturation. In other words, in this state, the piezomagnetic coefficient and
the permeability of the magnetostrictive composite are approximately constant. In addition, the pre-
stress has little effect on the magnetic flux density once the magnetization saturation $\left.|\bar{B}_1|\right|_{\max} \approx \pm 1\text{T}$.

This is attributed to the fact that the magnetic flux density is defined as $B_i = \mu_0 (H_i + M_i)$, where

the maximum magnetic flux density is only determined by the saturation magnetization that depends
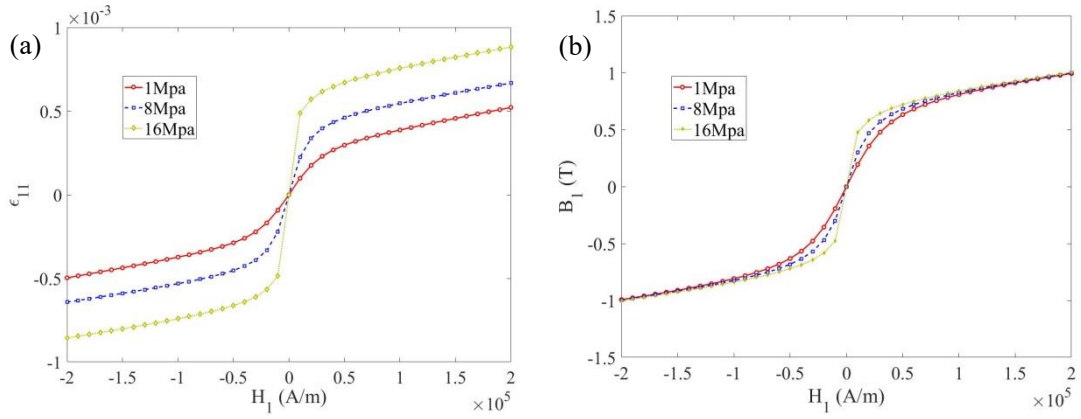on material properties, and has little correlation with pre-stress.

Fig. 7. Comparisons of the nonlinear responses with respect to the magnetic field intensity H_1 under different pre-stresses $\bar{\sigma}_{11}$ at reference temperature $T = T_0$ (a) Axial macroscopic strain $\bar{\varepsilon}_{11}$, and (b) Macroscopic magnetic flux density $\bar{B}_1$.

Fig. 8 shows the nonlinear responses of the equivalent piezomagnetic coefficient q_{11}^* and relative permeability μ_{11}^*/μ_0 with respect to magnetic field intensity H_1 under different axial pre-stresses $\bar{\sigma}_{11}$ when the fiber volume ratio is equal to 0.35. Due to the mechanical-magnetic coupling effects, the pre-contraction phenomenon along the Terfenol-D fiber direction occurs owing to the magnetic domain rotation before the magnetic field is applied. The minimum equivalent piezomagnetic coefficient q_{11}^* is equal to 62.1 N/Am, which is independent of the applied pre-stresses. The piezomagnetic coupling coefficient q_{11}^* starts to increase once a magnetic field is applied. It is worth noting that the equivalent piezomagnetic coefficient q_{11}^* is always positively correlated with the intensity of magnetic field, and tends to stabilize after saturation magnetization. It can be seen from Fig. 8 (b) that the relative permeability μ_{11}^*/μ_0 decreases sharply with the increase of magnetic field intensity. Moreover, the applied pre-stress tends to decrease the relative permeability to some extent, which is attributable to the internal compression that reduces magnetic field conduction.
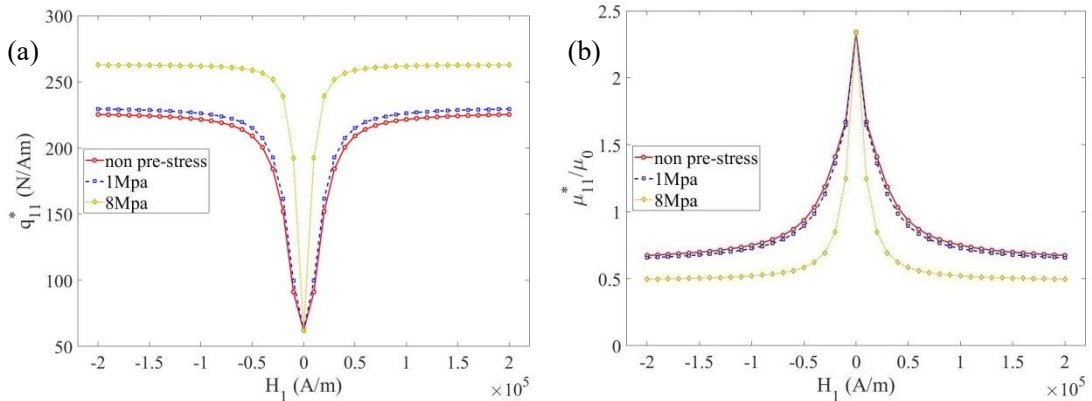
Fig. 8. Nonlinear property of the magnetostrictive composites with respect to magnetic field intensity H_1 under different pre-stresses $\bar{\sigma}_{11}$ at reference temperature $T = T_0$: (a) Equivalent piezomagnetic coefficient q_{11}^* (b) Relative permeability μ_{11}^*/μ_0

The local stress and strain distributions in the RVE predicted by the parametric FVDAM are shown in Fig. 9 for the magnetostrictive composites subjected to a magnetic field of intensity $H_1 = 100\text{kA/m}$ along the $x_1 - \text{direction}$ without considering any pre-stresses. In the figure, the strain distributions of ε_{22} and ε_{33} are identical due to symmetry and the effective stress is the von Mises stress given below.

$$\sigma_{\text{eff}} = \sqrt{\frac{1}{2}\left[\sigma_{11} - \sigma_{22}\right]^2 + \frac{1}{2}\left[\sigma_{22} - \sigma_{33}\right]^2 + \frac{1}{2}\left[\sigma_{33} - \sigma_{11}\right]^2} \tag{39}$$

It can be seen that higher microscopic stresses and strains are predicted when the nonlinear constitutive relationship is considered for the magnetostrictive composites. When the axial stress σ_{11} produced by the magnetic field intensity H_1 is considered, the fiber and the matrix sub-cells are, respectively, subjected to compression and tension. This is attributed to the mismatch of elastic modulus between the two materials. In addition, the maximum strain components ε_{22} and ε_{23} in the matrices are always located at the interface between the Terfenol-D fiber and the matrix materials. In details, the respective maximum transverse compressive strains $\varepsilon_{22}^{\text{max}}$ with and without considering nonlinearity are approximately -1.08×10^{-3} and -3.63×10^{-4}, which occurs around the interface in the matrix. The transverse compressive strains ε_{22} at the center distributed in the Terfenol-D fiber are 6.46×10^{-4} and 7.26×10^{-5}, respectively, from the nonlinear and linear analyses, which are lower than the transverse compressive strains along the matrix boundary. With and without considering nonlinearity, the respective maximum shear strains $\varepsilon_{23}^{\text{max}}$ are 7.06×10^{-4} and 1.84×10^{-4}. Due to the structural symmetry of the RVE model along the fiber direction, as shown in Fig. 1 (b), the maximum and minimum shear strains $\varepsilon_{23}^{\text{max}}$ and $\varepsilon_{23}^{\text{min}}$ are symmetrically distributed in the matrix, as shown in Fig. 9. In addition, the shear strains ε_{23} in the fiber is approximately zero because the fiber has a much greater elastic modulus than the matrix.

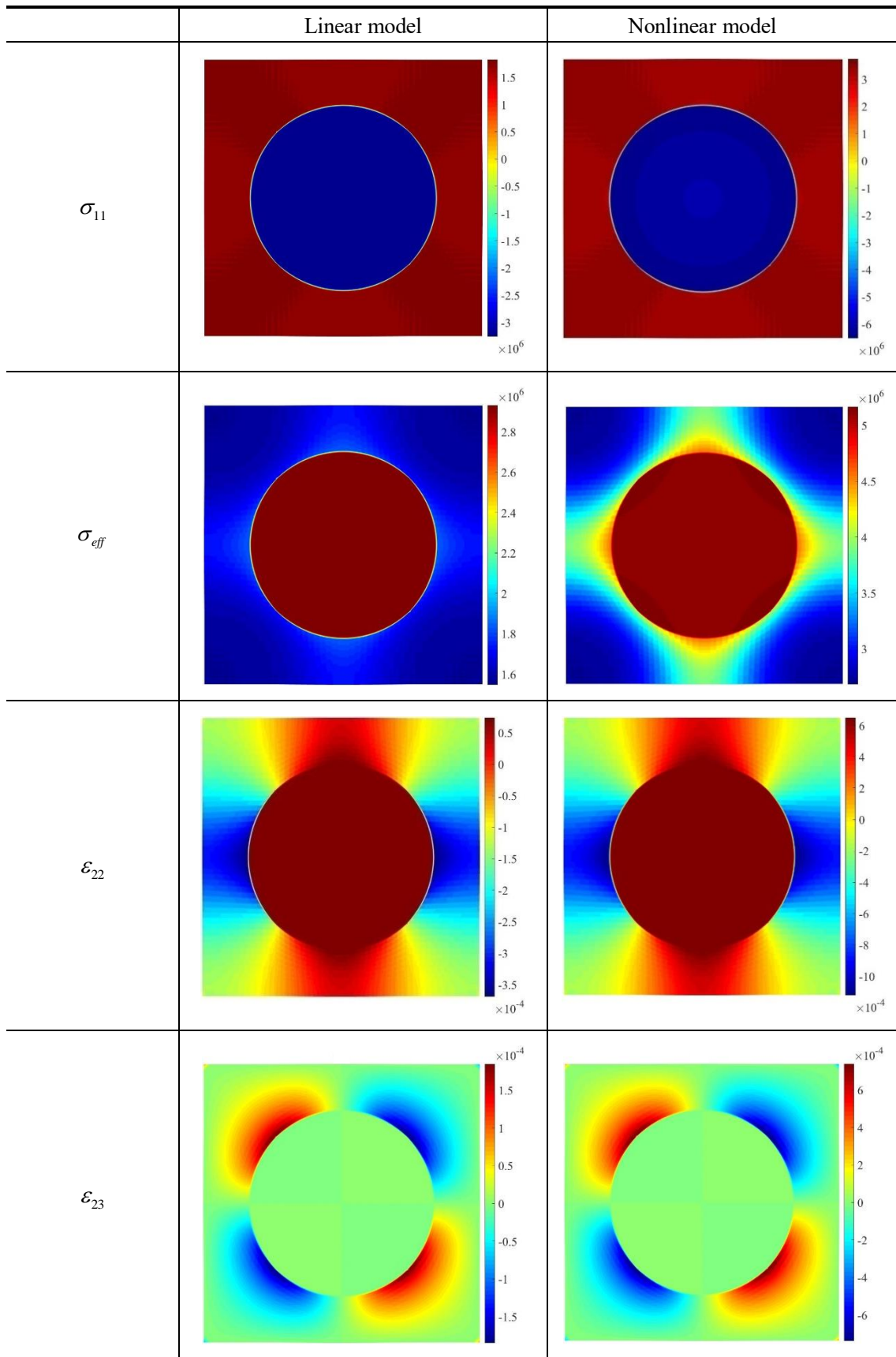|	Linear model	Nonlinear model
σ_{11}		
σ_{eff}		
ε_{22}		
ε_{23}		

Fig. 9. Comparisons of the local stress and strain distributions by the proposed FVDAM model with and without consideration of the nonlinear behaviors under an axial magnetic field intensity loading $H_1 = 100\text{kA/m}$.

Fig. 10 presents a comparison of the numerical results for the magnetostrictive composites with and without consideration of the nonlinear constitutive relation. Herein the magnetic flux density along fiber direction from -2×10^5 to 2×10^5 A/m is applied on. It can be observed from Fig. 10 (a) that the nonlinear model predicts higher strain amplitude before magnetization saturation. The linear and nonlinear numerical results shown in Fig. 10(b) are the macroscopic magnetic flux density $\bar{B}_1$ of the magnetostrictive composite when a magnetic field is applied on. With consideration of nonlinear properties, the magnetic flux density $\bar{B}_1$ of the magnetostrictive composite shows a rapid growth when $|H_1| \leq 60 \mathrm{kA/m}$. Once the magnetostrictive composite is at a saturation magnetization state, the growth rate of the magnetic flux density $\bar{B}_1$ is approximately a constant, showing an almost linear relation to magnetic field intensity.
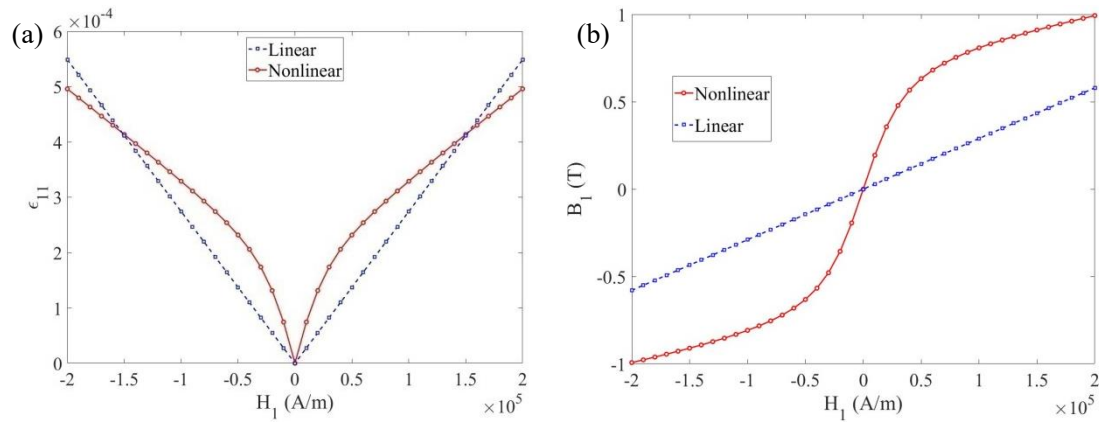

Fig. 10. Comparisons of the axial strain and magnetic flux density with respect to the nonlinear and linear constitutive relations (a) Axial macroscopic strain $\bar{\varepsilon}_{11}$, and (b) Macroscopic magnetic flux density $\bar{B}_1$.

Fig. 11 shows the effect of fiber volume fraction ($V_f = 0.35, 0.46,$ and 0.7) on the equivalent piezomagnetic coefficient q_{11}^*, relative permeability μ_{11}^*/μ_0 and axial increment strain $\Delta\bar{\varepsilon}_{11}$. A pre-stress of $\bar{\sigma}_{11} = 1 \mathrm{Mpa}$ is applied on the magnetostrictive composite at reference temperature $T_0 = 293\mathrm{K}$. It can be seen from Figs. 11(a) and (b) that under the same magnetic field the equivalent piezomagnetic coefficient and the relative permeability increase with the increase of fiber volume fraction. In addition, a higher equivalent piezomagnetic coefficient will generate more magnetostrictive strain, as shown in Fig. 11(c). The composite fiber ratio 0.7 has the highest strain.
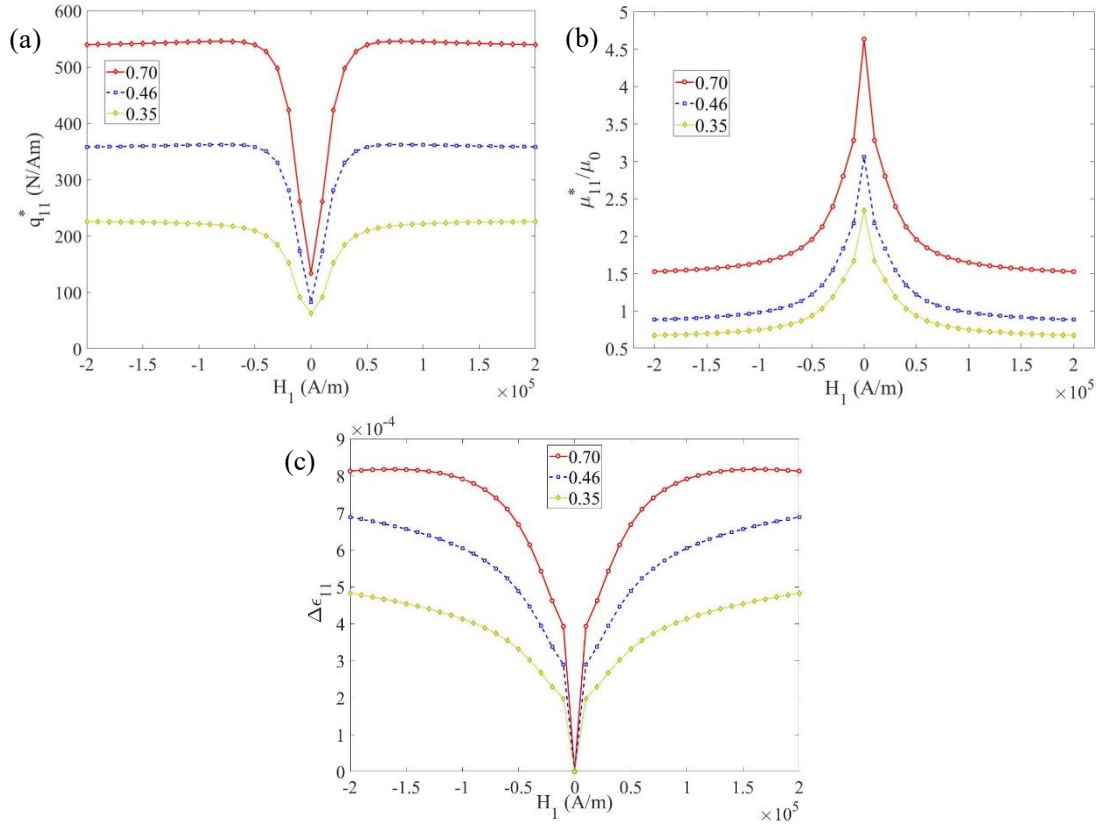
Fig. 11. Comparisons of the different fiber volume fraction ($V_f = 0.35$, 0.46, and 0.7) under pre-stress $\bar{\sigma}_{11} = 1$Mpa at reference temperature $T = T_0$ (a) Equivalent piezomagnetic coefficient q_{11}^*, (b) Relative permeability μ_{11}^*/μ_0 , and (c) Increment of axial strain $\Delta\bar{\varepsilon}_{11}$.

Fig. 12 shows the nonlinear magnetostrictive responses with respect to the axial strain $\Delta\bar{\varepsilon}_{11}$ and magnetic flux density B_1, respectively, at different ambient temperature changes. It can be seen from Fig. 12(a) that the axial magnetostrictive strain $\Delta\bar{\varepsilon}_{11}$ decreases with the increase of temperature change. Fig. 12(b) is the relation between the magnetic flux density B_1 and the temperature change. It is interesting to note that the temperature change ΔT has little effect on the magnetic flux density B_1.
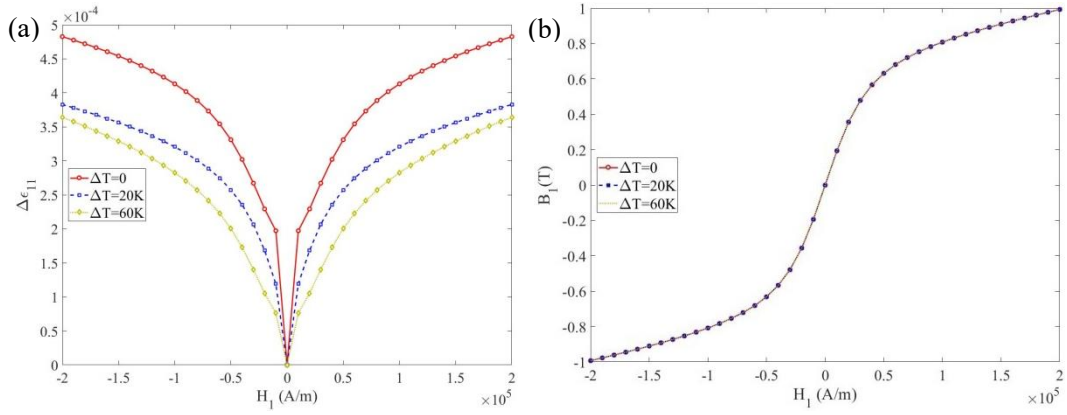
Fig. 12. Nonlinear magnetostrictive responses with respect to different temperature variations $\Delta T = T - T_0$: (a) Axial strain $\Delta \bar{\varepsilon}_{11}$ and (b) Magnetic flux density B_1.

Fig. 13 plots the equivalent piezomagnetic coefficient q_{11}^* and relative permeability μ_{11}^*/μ_0 of the magnetostrictive composite with respect to temperature changes ($\Delta T = T - T_0$). The results show that an elevated temperature has a negative impact on the magnetization process of the magnetostrictive fibers. This may be attributed to the suppressed rotation and movement of the magnetic domain. In other words, a magnetostrictive composite may not be suitable for an engineering application at a high ambient temperature. In general, the correlations of the influences of magnetic field, material composition and ambient temperature should be considered in the design procedure of magnetostrictive composites.
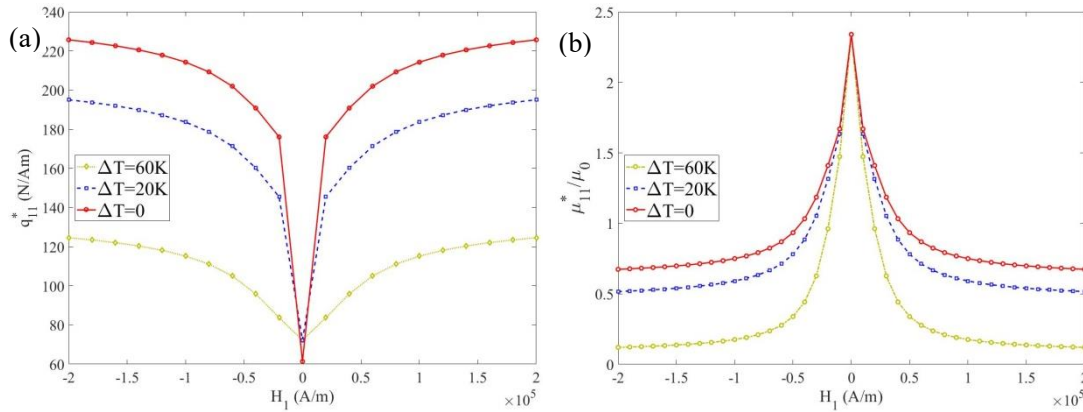

Fig. 13. Effective properties of magnetostrictive composites with respect to temperature changes $\Delta T = T - T_0$ (a) Equivalent piezomagnetic coefficient q_{11}^* and (b) Relative permeability μ_{11}^*/μ_0.

5. Conclusions

This paper presented a nonlinear microscopic constitutive model to effectively describe the mechanical behaviors of magnetostrictive composites subjected to coupled mechanical-magneto-thermal conditions. By discretizing the RVE with the constructed parametric sub-cells, the proposed model shows a good ability in capturing nonlinear responses of the magnetostrictive composites with different fiber volume fraction and ambient temperature, etc. The main conclusions of this study are summarized as follows:

1) The proposed nonlinear constitutive model is sufficiently accurate in investigating the effective nonlinear properties of the magnetostrictive composites.

2) The nonlinear variations of strain and flux density are closely related to magnetization intensity and approach to a steady state after saturation of magnetization. The maximum saturation point in the magnetization process closely depends on the properties of the constituent materials, which has little correlation with the pre-stress and ambient temperature.

3) Pre-stresses and temperature affect magnetostrictive strain and magnetic flux density by influencing the equivalent piezomagnetic coefficient and permeability. Pre-stress causes sharply increase of the piezomagnetic coefficient, which further results in a higher strain amplitude. In addition, a higher temperature variation can inhibit the equivalent piezomagnetic coefficient.

4) Before saturation of magnetization, the strain responses of material with consideration of nonlinearity are higher than those without. Moreover, the nonlinear results are consistent with experiment results.

In summarize, the proposed micromechanical method is capable of investigating nonlinear performance of magnetostrictive composites, which is useful in design and application of the materials. In addition, the proposed micromechanical model based on the nonlinear constitutive equation can be developed to model particulate magnetostrictive composites.

Data availability statement

The raw/processed data required to reproduce these findings cannot be shared at this time as the data also forms part of an ongoing study.

CRediT authorship contribution statement

Ziwei Li: Writing-original draft, Methodology, Visualization. **Junjie Ye:** Writing-original draft, Methodology, Conceptualisation.**Yiwei Wang:** Visualization, Methodology. **Lu Liu**: Validation, Data curation; **Yang Shi**: Methodology, Visualization, Data curation.**Yang Li**: Resources, Data curation.**Jianqiao Ye:** Methodology, Conceptualisation, Writing-review & editing, Supervision.

Declaration of Competing Interest

The authors declare that they have no known competing financial interests or personal relationships that could have appeared to influence the work reported in this paper.

Appendix 1

$$\mathbf{A} = \begin{bmatrix} \dfrac{1}{E} + \dfrac{\lambda_s}{\sigma_s} - \dfrac{\lambda_s M_1^2}{\sigma_s M_s^2} & -\dfrac{v}{E} - \dfrac{\lambda_s}{2\sigma_s} + \dfrac{\lambda_s M_2^2}{2\sigma_s M_s^2} & -\dfrac{v}{E} - \dfrac{\lambda_s}{2\sigma_s} + \dfrac{\lambda_s M_3^2}{2\sigma_s M_s^2} \\[2ex] -\dfrac{v}{E} - \dfrac{\lambda_s}{2\sigma_s} + \dfrac{\lambda_s M_1^2}{2\sigma_s M_s^2} & \dfrac{1}{E} + \dfrac{\lambda_s}{\sigma_s} - \dfrac{\lambda_s M_2^2}{\sigma_s M_s^2} & -\dfrac{v}{E} - \dfrac{\lambda_s}{2\sigma_s} + \dfrac{\lambda_s M_3^2}{2\sigma_s M_s^2} \\[2ex] -\dfrac{v}{E} - \dfrac{\lambda_s}{2\sigma_s} + \dfrac{\lambda_s M_1^2}{2\sigma_s M_s^2} & -\dfrac{v}{E} - \dfrac{\lambda_s}{2\sigma_s} + \dfrac{\lambda_s M_2^2}{2\sigma_s M_s^2} & \dfrac{1}{E} + \dfrac{\lambda_s}{\sigma_s} - \dfrac{\lambda_s M_3^2}{\sigma_s M_s^2} \end{bmatrix}$$

$$\mathbf{B} = \begin{bmatrix} \dfrac{1+v}{2E} + \dfrac{3\lambda_s}{4\sigma_s} - \dfrac{3\lambda_s M_2^2}{4M_s^2} & 0 & 0 \\[2ex] 0 & \dfrac{1+v}{2E} + \dfrac{3\lambda_s}{4\sigma_s} - \dfrac{3\lambda_s M_1^2}{4M_s^2} & 0 \\[2ex] 0 & 0 & \dfrac{1+v}{2E} + \dfrac{3\lambda_s}{4\sigma_s} - \dfrac{3\lambda_s M_1^2}{4M_s^2} \end{bmatrix}$$

$$\mathbf{C} = \begin{bmatrix} \dfrac{M_1}{M_s^2}\left[2\lambda_s + 2\bar{\beta}\Delta T - \dfrac{2\lambda_s \sigma_{11}}{\sigma_s} \right] & \dfrac{M_2}{M_s^2}\left[-\lambda_s + 2\bar{\beta}\Delta T - \dfrac{3\lambda_s \sigma_{11} - \lambda_s \sigma_{22}}{\sigma_s} \right] & \dfrac{M_2}{M_s^2}\left[-\lambda_s + 2\bar{\beta}\Delta T - \dfrac{3\lambda_s \sigma_{11} - \lambda_s \sigma_{22}}{\sigma_s} \right] \\[3ex] \dfrac{M_1}{M_s^2}\left[-\lambda_s + 2\bar{\beta}\Delta T - \dfrac{3\lambda_s \sigma_{22} - \lambda_s \sigma_{11}}{\sigma_s} \right] & \dfrac{M_2}{M_s^2}\left[2\lambda_s + 2\bar{\beta}\Delta T - \dfrac{2\lambda_s \sigma_{22}}{\sigma_s} \right] & \dfrac{M_3}{M_s^2}\left[-\lambda_s + 2\bar{\beta}\Delta T - \dfrac{3\lambda_s \sigma_{22} - \lambda_s \sigma_{33}}{\sigma_s} \right] \\[3ex] \dfrac{M_1}{M_s^2}\left[-\lambda_s + 2\bar{\beta}\Delta T - \dfrac{3\lambda_s \sigma_{33} - \lambda_s \sigma_{11}}{\sigma_s} \right] & \dfrac{M_2}{M_s^2}\left[-\lambda_s + 2\bar{\beta}\Delta T - \dfrac{3\lambda_s \sigma_{33} - \lambda_s \sigma_{22}}{\sigma_s} \right] & \dfrac{M_3}{M_s^2}\left[2\lambda_s + 2\bar{\beta}\Delta T - \dfrac{2\lambda_s \sigma_{33}}{\sigma_s} \right] \end{bmatrix}$$

$$\mathbf{D} = \begin{bmatrix} \dfrac{1}{k(\theta)} \dfrac{\pi}{2M_s} \sec^2\!\left(\dfrac{\pi M_1}{2M_s} \right) - \dfrac{3\left(\sigma_{11} - \sigma_S \ln\!\left[\dfrac{2\sqrt{2}}{3}\cosh\!\left(\dfrac{\sigma_{11}}{\sigma_s} \right) \right] \right)}{\mu_0 (M_s)^2} M_1 \\[4ex] \dfrac{1}{k(\theta)} \dfrac{\pi}{2M_s} \sec^2\!\left(\dfrac{\pi M_2}{2M_s} \right) - \dfrac{3\left(\sigma_{22} - \sigma_S \ln\!\left[\dfrac{2\sqrt{2}}{3}\cosh\!\left(\dfrac{\sigma_{22}}{\sigma_s} \right) \right] \right)}{\mu_0 (M_s)^2} M_2 \\[4ex] \dfrac{1}{k(\theta)} \dfrac{\pi}{2M_s} \sec^2\!\left(\dfrac{\pi M_3}{2M_s} \right) - \dfrac{3\left(\sigma_{22} - \sigma_S \ln\!\left[\dfrac{2\sqrt{2}}{3}\cosh\!\left(\dfrac{\sigma_{22}}{\sigma_s} \right) \right] \right)}{\mu_0 (M_s)^2} M_3 \end{bmatrix}$$

$$\mathbf{R_1} = \begin{bmatrix} \bar{\alpha} + \dfrac{M_1^2 \bar{\beta}}{M_s^2} \\[2ex] \bar{\alpha} + \dfrac{M_2^2 \bar{\beta}}{M_s^2} \\[2ex] \bar{\alpha} + \dfrac{M_3^2 \bar{\beta}}{M_s^2} \\[2ex] 0 \\[1ex] 0 \\[1ex] 0 \end{bmatrix} \qquad \mathbf{R_2} = \begin{bmatrix} \dfrac{2\bar{\beta}\sigma_{11}M_1}{M_s^2} \\[2ex] \dfrac{2\bar{\beta}\sigma_{22}M_2}{M_s^2} \\[2ex] \dfrac{2\bar{\beta}\sigma_{33}M_3}{M_s^2} \end{bmatrix}$$

Appendix 2

$$\mathbf{E_1} = \begin{bmatrix} 0 & 0 & 0 & 0 & 0 & 0 & 0 & 0 \\ 0 & 0 & 1 & 3 & 0 & 0 & 0 & 0 \\ 0 & 0 & 1 & 3 & 0 & 0 & 0 & 0 \\ 0 & 0 & 1 & 3 & 1 & 3 & 0 & 0 \\ 1 & 3 & 0 & 0 & 0 & 0 & 0 & 0 \\ 1 & 3 & 0 & 0 & 0 & 0 & 0 & 0 \\ 0 & 0 & 0 & 0 & 0 & 0 & 0 & 0 \\ 0 & 0 & 0 & 0 & 0 & 0 & 1 & 3 \\ 0 & 0 & 0 & 0 & 0 & 0 & 1 & 3 \end{bmatrix} \quad \mathbf{E_2} = \begin{bmatrix} 0 & 0 & 0 & 0 & 0 & 0 & 0 & 0 \\ 0 & 0 & 1 & -3 & 0 & 0 & 0 & 0 \\ 0 & 0 & 1 & -3 & 0 & 0 & 0 & 0 \\ 0 & 0 & 1 & -3 & 1 & -3 & 0 & 0 \\ 1 & -3 & 0 & 0 & 0 & 0 & 0 & 0 \\ 1 & -3 & 0 & 0 & 0 & 0 & 0 & 0 \\ 0 & 0 & 0 & 0 & 0 & 0 & 0 & 0 \\ 0 & 0 & 0 & 0 & 0 & 0 & 1 & -3 \\ 0 & 0 & 0 & 0 & 0 & 0 & 1 & -3 \end{bmatrix}$$

$$\mathbf{W_1} = \begin{bmatrix} \Delta W_{1(01)} \\ \Delta W_{1(02)} \\ \Delta W_{2(01)} \\ \Delta W_{2(02)} \\ \Delta W_{3(01)} \\ \Delta W_{3(02)} \\ \Delta W_{4(01)} \\ \Delta W_{4(02)} \end{bmatrix} \quad \mathbf{J_1} = \begin{bmatrix} J_{23} \\ J_{33} \\ J_{23} \\ J_{33} \\ J_{33} \\ J_{23} \\ J_{23} \\ J_{33} \end{bmatrix}^T \quad \mathbf{W_2} = \begin{bmatrix} \Delta W_{1(10)} \\ \Delta W_{1(20)} \\ \Delta W_{2(10)} \\ \Delta W_{2(20)} \\ \Delta W_{3(10)} \\ \Delta W_{3(20)} \\ \Delta W_{4(10)} \\ \Delta W_{4(20)} \end{bmatrix} \quad \mathbf{J_2} = \begin{bmatrix} J_{22} \\ J_{32} \\ J_{22} \\ J_{32} \\ J_{32} \\ J_{22} \\ J_{22} \\ J_{32} \end{bmatrix}^T$$

References

[1]   Olabi AG, Grunwald A. Design and application of magnetostrictive materials. Materials and Design 2008;29:469–83. https://doi.org/10.1016/j.matdes.2006.12.016.

[2]   Jiles DC, Thoelke JB. Magnetization and Magnetostriction in Terbium–Dysprosium–Iron Alloys. Physica Status Solidi (A) 1995;147:535–51. https://doi.org/10.1002/pssa.2211470224.

[3]   Nersessian N, Or SW, Carman GP. Magneto-thermo-mechanical characterization of 1-3 type polymer-bonded Terfenol-D composites. Journal of Magnetism and Magnetic Materials 2003;263:101–12. https://doi.org/10.1016/S0304-8853(02)01542-1.

[4]   Moffett MB, Clark AE, Wun-Fogle M, Lindberg JF, Teter JP, McLaughlin EA. Characterization of Terfenol-D for magnetostrictive transducers. The Journal of the Acoustical Society of America 1990;87:S95–S95. https://doi.org/10.1121/1.2028440.

[5]   Carman GP, Mitrovic M. Nonlinear Constitutive Relations for Magnetostrictive Materials with Applications to 1-D Problems 1994:673–83.

[6]   Wan Y, Fang D, Soh AK, Hwang KC. Experimental and theoretical study of the nonlinear response of a giant magnetostrictive rod. Acta Mechanica Sinica/Lixue Xuebao 2003;19:324–9. https://doi.org/10.1007/bf02487809.

[7]   Wan Y, Fang D, Hwang KC. Non-linear constitutive relations for magnetostrictive materials. International Journal of Non-Linear Mechanics 2003;38:1053–65. https://doi.org/10.1016/S0020-7462(02)00052-5.

[8]   Duenas TA, Hsu L, Carman GP. Magnetostrictive composite material systems analytical/experimental. Materials Research Society Symposium - Proceedings 1997;459:527–43. https://doi.org/10.1557/proc-459-527.

[9]   Zheng XJ, Liu XE. A nonlinear constitutive model for Terfenol-D rods. Journal of App

lied Physics 2005;97. https://doi.org/10.1063/1.1850618.

[10]   Liu X, Zheng X. Nonlinear constitutive model for magnetostrictive materials. Acta Mec
hanica Sinica/Lixue Xuebao 2005;21:278–85. https://doi.org/10.1007/s10409-005-0028-8.

[11]   Jin K, Kou Y, Liang Y, Zheng X. Effects of hysteresis losses on dynamic behavior of
magnetostrictive actuators. Journal of Applied Physics 2011;110. https://doi.org/10.1063/1.
3656981.

[12]   Elhajjar R, Law CT, Pegoretti A. Magnetostrictive polymer composites: Recent advances
in materials, structures and properties. Progress in Materials Science 2018;97:204–29. h
ttps://doi.org/10.1016/j.pmatsci.2018.02.005.

[13]   Kaleta J, Lewandowski D, Mech R. Magnetomechanical properties of magnetostrictive c
omposites with high volume of fraction Terfenol-D powder. Behavior and Mechanics of
Multifunctional Materials and Composites 2010 2010;7644:76441L. https://doi.org/10.1117
/12.847845.

[14]   Herbst JF, Capehart TW, Pinkerton FE. Estimating the effective magnetostriction of a c
omposite: A simple model. Applied Physics Letters 1997;70:3041–3. https://doi.org/10.10
63/1.118743.

[15]   Nan CW. Effective magnetostriction of magnetostrictive composites. Applied Physics Let
ters 1998;72:2897–9. https://doi.org/10.1063/1.121452.

[16]   Nan CW, Weng GJ. Influence of microstructural features on the effective magnetostricti
on of composite materials. Physical Review B - Condensed Matter and Materials Physic
s 1999;60:6723–30. https://doi.org/10.1103/PhysRevB.60.6723.

[17]   Liu LP, James RD, Leo PH. Magnetostrictive composites in the dilute limit. Journal of
the Mechanics and Physics of Solids 2006;54:951–74. https://doi.org/10.1016/j.jmps.2005.
11.006.

[18]   Tang T, Myers O, Felicelli SD. Computational prediction of effective magnetostriction a
nd moduli of multiphase magnetostrictive composites. International Journal of Engineerin
g Science 2013;72:1–10. https://doi.org/10.1016/j.ijengsci.2013.06.008.

[19]   Yifeng Z, Lei C, Yu W, Xiaoping Z. Variational asymptotic micromechanics modeling
of heterogeneous magnetostrictive composite materials. Composite Structures 2013;106:50
2–9. https://doi.org/10.1016/j.compstruct.2013.06.018.

[20]   Xue L, Mu H, Sun Y. Micromechanical model for the ferromagnetic shape memory all
oy-epoxy resin composite considering variant reorientation and magneto-mechanical coup
ling. Journal of the Mechanical Behavior of Biomedical Materials 2021;117. https://doi.o
rg/10.1016/j.jmbbm.2021.104396.

[21]   Guan X, Dong X, Ou J. Predicting performance of polymer-bonded Terfenol-D composi
tes under different magnetic fields. Journal of Magnetism and Magnetic Materials 2009;
321:2742–8. https://doi.org/10.1016/j.jmmm.2009.03.084.

[22]   Bansal Y, Pindera MJ. Finite-volume direct averaging micromechanics of heterogeneous
materials with elastic-plastic phases. International Journal of Plasticity 2006;22:775–825.
https://doi.org/10.1016/j.ijplas.2005.04.012.

[23]   Bansal Y, Pindera MJ. A second look at the higher-order theory for periodic multiphas
e materials. Journal of Applied Mechanics, Transactions ASME 2005;72:177–95. https://
doi.org/10.1115/1.1831294.

[24]   Khatam H, Pindera MJ. Parametric finite-volume micromechanics of periodic materials

with elastoplastic phases. International Journal of Plasticity 2009;25:1386–411. https://doi.org/10.1016/j.ijplas.2008.09.003.

[25] Cavalcante MAA, Marques SPC, Pindera MJ. Parametric formulation of the finite-volume theory for functionally graded materials - Part I: Analysis. Journal of Applied Mechanics, Transactions ASME 2007;74:935–45. https://doi.org/10.1115/1.2722312.

[26] Li Z, Ye J, Liu L, Cai H, He WP, Cai G, et al. Evaluation of piezoelectric and mechanical properties of the piezoelectric composites with local damages. Mechanics of Advanced Materials and Structures 2021;0:1–25. https://doi.org/10.1080/15376494.2021.1901322.

[27] Ye J, Cai H, Liu L, Zhai Z, Amaechi CV, Wang Y, et al. Microscale intrinsic properties of hybrid unidirectional/woven composite laminates: Part I experimental tests. Composite Structures 2020;262:113369. https://doi.org/10.1016/j.compstruct.2020.113369.

[28] Ye J, Wang Y, Li Z, Saafi M, Jia F, Huang B, et al. Failure analysis of fiber-reinforced composites subjected to coupled thermo-mechanical loading. Composite Structures 2020;235. https://doi.org/10.1016/j.compstruct.2019.111756.

[29] Cai H, Ye J, Shi J, Wang Y, Shi Y, Huang B, et al. A new two-step modeling strategy for random micro-fiber reinforced composites with consideration of primary pores. Composites Science and Technology 2022;218:109122. https://doi.org/10.1016/j.compscitech.2021.109122.

[30] Chen Q, Wang G. Homogenized and localized responses of coated magnetostrictive porous materials and structures. Composite Structures 2018;187:102–15. https://doi.org/10.1016/j.compstruct.2017.12.032.

[31] Jin K, Kou Y, Zheng X. The resonance frequency shift characteristic of Terfenol-D rods for magnetostrictive actuators. Smart Materials and Structures 2012;21. https://doi.org/10.1088/0964-1726/21/4/045020.

[32] Charalambakis N. Homogenization techniques and micromechanics. A survey and perspectives. Applied Mechanics Reviews 2010;63:1–10. https://doi.org/10.1115/1.4001911.

[33] Hill R. Elastic properties of reinforced solids: Some theoretical principles. Journal of the Mechanics and Physics of Solids 1963;11:357–72.https://doi.org/10.1016/0022-5096(63)90036-X.

[34] Zhan YS, Lin C hong. Micromechanics-based constitutive modeling of magnetostrictive 1–3 and 0–3 composites. Composite Structures2021;260:1–16.https://doi.org/10.1016/j.compstruct.2020.113264.

[35] Mech R, Kaleta J. Influence of Terfenol-D powder volume fraction in epoxy matirx composites on their magnetomechanical properies. Acta Mechanica et Automatica 2017;11:233–6. https://doi.org/10.1515/ama-2017-0036.